nature communications

Article

https://doi.org/10.1038/s41467-025-66750-4

Interacting filaments drive vesicle morphogenesis

Received: 22 February 2025

Accepted: 13 November 2025

Chengyao Zhang[1,3], Guijin Zou[2,3], Yaxin Fang[1], Huajian Gao[2] & Xin Yi[1]

The interplay between vesicles and their enclosed filaments is fundamental to the morphogenesis, motility, and mechanical response of biological cells, artificial cells, and biomimetic robotic systems. By engineering responsiveness or interaction capabilities—such as long-range filament interactions—these filaments can function as active elements that regulate system behavior. Here, we combine theoretical modeling and molecular dynamics simulations to demonstrate how interacting filament loops within vesicles induce diverse, system-wide morphological transformations. These transformations are driven by inter- and intrafilament interactions, as well as the competing deformations of both the vesicle and its encapsulated filaments, with interfilament interactions playing a dominant role. We observe phenomena including filament buckling and reorientation, vesicle stretching, and convex-to-concave shape transitions. Morphological phase diagrams are constructed for both vesicles under zero osmotic pressure and those with a fixed relative volume, and we further explore the packing of inhomogeneous filament loops. These results offer quantitative design principles for artificial cellular systems in which filament interactions act as levers to control and stabilize emergent morphologies, laying the groundwork for the development of adaptive soft robotics.

The interplay between deformable membranes and enclosed filaments governs key aspects of morphogenesis, motility, and mechanical adaptability in biological cells as well as in vesicle-based artificial cellular systems[1,2]. From a mechanical perspective, cells and vesicles encapsulate the fundamental physics of membrane-mediated confinement[3–5], while their enclosed filamentous components—whether cytoskeletal polymers, nucleated microtubules, or engineered materials—act as structural and functional scaffolds that regulate system-wide behavior through mechanical and biophysical feedback. In living cells, this physical dialogue manifests in diverse processes such as microtubule-driven platelet activation[6], actin-mediated pseudopod formation during cell locomotion[1], and membrane tubulation in cell uptake[7]. Synthetic analogs such as vesicles encapsulating actin filaments and microtubules[8–15], or self-propelled rigid rods and cargoes[16–20], recapitulate similar behaviors on similar length scales yet with reduced biological complexity. These systems offer valuable platforms for uncovering design principles of shape-programmable structures with potential applications in artificial cells. Recent theoretical advances have established a full spectrum of packing morphologies for single flexible filaments—both open and closed—within vesicles, delineating the conditions for transitions between configurations[21–23].

While these investigations have provided valuable insights, a key unresolved question is how competing energy hierarchies—spanning filament flexibility, tunable interfilament interactions, and membrane deformation—collaborate to orchestrate and stabilize morphological transitions in filaments–vesicle systems. Understanding these interactions is essential for bridging the gap between the inherent complexity of biological systems and the rational design of synthetic cellular systems. Notably, long-range interfilament interactions (e.g.,

---

[1]School of Mechanics and Engineering Science, Peking University, Beijing, China. [2]Mechano-X Institute, Department of Engineering Mechanics, Tsinghua University, Beijing, China. [3]These authors contributed equally: Chengyao Zhang, Guijin Zou. e-mail: gao.huajian@tsinghua.edu.cn; xyi@pku.edu.cn

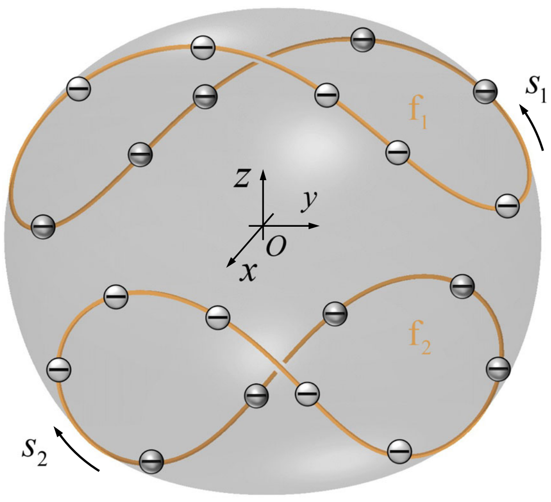

Fig. 1 | Schematic of two charged filament loops confined within a vesicle of effective radius *R*. The filaments f_1 and f_2, carrying like electrical charges (e.g., negative here), repel each other, resulting in a competition between repulsive intra- and interfilament interactions and the elastic deformation of both the filaments and the confining vesicle.

electrostatic forces), which are prevalent in biological processes like polyelectrolyte condensation[24,25] and viral genome packaging[26,27], remain underexplored in the context of vesicle morphogenesis.

In this work, we employ theoretical modeling and molecular dynamics (MD) simulations to elucidate the mechanisms underlying vesicle morphogenesis driven by enclosed flexible filament loops, with long-range interactions capturing both inter- and intrafilament forces. We systematically explore how variations in filament stiffness, length, and interaction strength influence system morphologies in vesicles under zero osmotic pressure or maintained a fixed volume. By establishing symmetry-based morphological categorizations and phase diagrams, we highlight key features such as filament buckling, reorientation, and vesicle stretching or inflation. Energy and membrane tension analysis further reveal the mechanical pathways driving these transitions. We also discuss possible implications of our results on programmable cellular systems.

Results

Model and parametrization

Consider two inextensible, uniformly charged filament loops, f_1 and f_2, confined within a lipid vesicle of fixed area $A(=4\pi R^2)$, where R is the effective vesicle radius. The vesicle can either freely adjust its volume at zero osmotic pressure difference ($\Delta p = 0$) or maintain a fixed volume V. Filaments f_1 and f_2 have lengths L_1 and L_2, respectively, and are uniformly charged with like charges (e.g., negative in Fig. 1) at densities λ_1 and λ_2. Here, electrostatic interactions are employed to model the tunable filament interaction. The nonlocal Coulomb interaction causes the filaments to repel each other, while the vesicle confinement imposes elastic and geometric constraints to the filaments. The competition between the repulsive Coulomb interaction and the bending resistance of the filaments and vesicle membrane leads to a complex morphological evolution of the filaments–vesicle system.

It is important to note that the electrostatic interaction here does not correspond to a specific physical mechanism, but rather serves as a generic, tunable model for long-range filament-filament interactions. This abstraction enables us to systematically probe how nonlocal repulsion modulates vesicle morphology. Experimentally, such interactions can be realized using stimulus-responsive microscale filaments, for example, through magnetic self-assembly of lipid-coated nanoparticles or electrospinning of magnetically or optically active polymers. Related experimental strategies and their relevance to our findings are further discussed in the "Discussion".

Throughout the main text, we focus on the long-range limit, corresponding to a salt-free environment where electrostatic interactions are effectively unscreened. This regime provides a simplified setting allowing us to isolate the conceptual role of unscreened electrostatics in filaments-vesicle organization. While not intended to replicate specific biological conditions, this limit serves as a reference point for understanding the qualitative role of interaction range in shaping vesicle morphology.

To assess the robustness of our findings with respect to this modeling assumption, we also perform simulations incorporating electrostatic screening, modeled via a screened Coulomb potential with an adjustable Debye length. The results on screening-dependent modulation are analyzed in detail in the "Discussion" and Supplementary Information. Briefly, we find that under weak screening, the filament configurations and vesicle morphologies remain qualitatively similar to those observed in the unscreened case, indicating that the shape transitions are robust against mild attenuation. In contrast, strong screening substantially reduces interfilament repulsion, requiring higher interaction strength to achieve comparable morphological changes.

The total system energy is $E_{\mathrm{tot}} = E_{\mathrm{m}} + E_{\mathrm{f}} + E_{\mathrm{intra}} + E_{\mathrm{inter}}$, consisting of the bending energy of the vesicle membrane E_{m}, bending energy of two filaments E_{f}, intrafilament interaction energy E_{intra}, and interfilament interaction energy E_{inter}. Adopting the Helfrich theory for the membrane[28], the wormlike chain model for the filaments[29], and the Coulomb's inverse-square law for interaction potentials, these four energy components are

$$
\begin{aligned}
E_{\mathrm{m}} &= 2\kappa \int H^2 \mathrm{d}A,\\
E_{\mathrm{f}} &= \frac{Y_1 I_1}{2}\int_0^{L_1} C_1^2 \mathrm{d}s_1 + \frac{Y_2 I_2}{2}\int_0^{L_2} C_2^2 \mathrm{d}s_2,\\
E_{\mathrm{intra}} &= \sum_{i=1,2} \frac{\lambda_i^2}{8\pi\varepsilon_0\varepsilon_{\mathrm{r}}}\int_0^{L_i}\int_0^{L_i} \frac{M}{|\mathbf{r}_i^{\mathrm{f}}(s_i) - \mathbf{r}_i^{\mathrm{f}}(\bar{s}_i)|}\mathrm{d}s_i \mathrm{d}\bar{s}_i,\\
E_{\mathrm{inter}} &= \frac{\lambda_1\lambda_2}{4\pi\varepsilon_0\varepsilon_{\mathrm{r}}}\int_0^{L_2}\int_0^{L_1} \frac{1}{|\mathbf{r}_1^{\mathrm{f}}(s_1) - \mathbf{r}_2^{\mathrm{f}}(s_2)|}\mathrm{d}s_1 \mathrm{d}s_2,
\end{aligned}
$$

where κ, H, and $\mathrm{d}A$ represent the bending rigidity, mean curvature, and surface element of the membrane, respectively; C_i is the local curvature of the filament f_i ($i = 1, 2$) modeled as a space curve with its centerline position vector $\mathbf{r}_i^{\mathrm{f}}(s_i)$, and Y_i, I_i, s_i, and $\mathrm{d}s_i$ denote the Young's modulus, moment of inertia, arclength, and curve element of the filament f_i, respectively; λ_i is the uniformly distributed charge density (per unit length), ε_0 is the vacuum permittivity, ε_{r} is the relative permittivity of the solvent (e.g., $\varepsilon_{\mathrm{r}} \approx 80$ for water at room temperature). Hereinafter, the subscripts 1 and 2 refer to quantities pertaining to filaments f_1 and f_2, respectively. In E_{intra}, a mollifier M is introduced to regularize the singular self-interaction electrostatic potential. A specific form is taken as $M = \eta_i^4/(\eta_i + e^{-7\eta_i})^4$ with $\eta_i = \sin(\pi|s_i - \bar{s}_i|/L_i)$[30,31]. For two circular charged filament loops infinitely far away from each other as a reference state, the corresponding intrafilament interaction energy is $E_{\mathrm{intra}}^0 = 0.1286(\lambda_1^2 L_1 + \lambda_2^2 L_2)/(\varepsilon_0\varepsilon_{\mathrm{r}})$.

For simplicity in the following analysis, we consider two identical filaments ($L_1 = L_2 = L$, $Y_1 I_1 = Y_2 I_2 = YI$, and $\lambda_1 = \lambda_2 = \lambda$) unless otherwise specified. At zero osmotic pressure ($\Delta p = 0$) or a given reduced vesicle volume $\upsilon = V/(4\pi R^3/3)$, the total system energy is

$$
E_{\mathrm{tot}} = E_{\mathrm{tot}}\left(YI/(\kappa R), L/(\pi R), \chi\right),
$$

a function of the relative stiffness $YI/(\kappa R)$ and length $L/(\pi R)$ of the filaments, as well as the dimensionless Coulomb interaction strength $\chi = \lambda^2 R/(4\pi\varepsilon_0\varepsilon_{\mathrm{r}}\kappa)$.

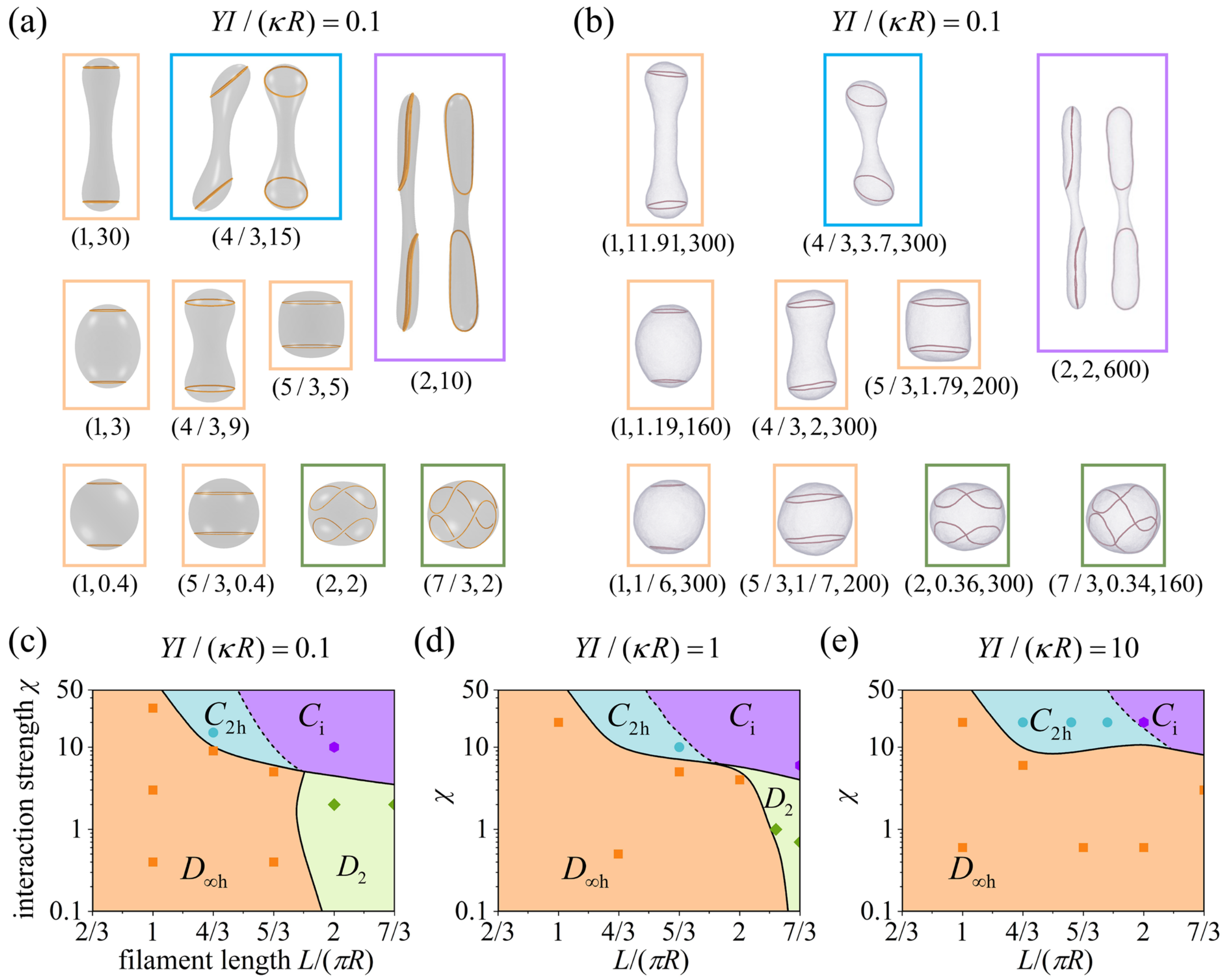

Fig. 2 | The interacting filaments–vesicle system at $\Delta p = 0$. Representative equilibrium system morphologies for highly flexible filaments ($YI/(\kappa R) = 0.1$) obtained from numerical optimization (**a**) and MD simulations (**b**). **c**–**e** Morphological phase diagrams in terms of $L/(\pi R)$ and χ for $YI/(\kappa R) = 0.1$, 1, and 10, respectively. In (**a**), respective values of $(L/(\pi R), \chi)$ are provided below each morphology. In (**b**), corresponding values of $(L/(\pi R), 1/\varepsilon_r, b_s/\Sigma)$ are displayed, where b_s is the simulation box size adjusted to accommodate elongated vesicles and Σ is the length unit in MD simulations. The length scales in (**a**) and (**b**) are identical. Symbols in **c**–**e** correspond to the framed morphologies in panel (**a**), Supplementary Fig. S7 and Fig. S8, respectively. The solid (dashed) phase boundaries denote discontinuous (continuous) morphological transitions.

Here, we employ both numerical optimization and MD simulations to identify the minimum energy state for a given set of parameters ($YI/(\kappa R)$, $L/(\pi R)$, χ), with methodological details in the Methods section and Supplementary Figs. S1–S4.

At $\Delta p = 0$, the spherical filament-free vesicle offers isotropic confinement. In contrast, when the vesicle's reduced volume υ is specified, its shape depends on υ: at $\upsilon = 1$, it is spherical, but as υ decreases, it transforms from prolate to oblate and then to a stomatocyte shape[32]. These nonspherical forms provide anisotropic confinement. The behavior of the interacting filaments–vesicle system under both the isotropic and anisotropic confinements is elucidated in the following analysis.

Interacting filaments–vesicle system at zero osmotic pressure difference

We first investigate system morphologies for highly flexible filaments ($YI/(\kappa R) = 0.1$) at $\Delta p = 0$ (Fig. 2), focusing on how filament-vesicle interactions are regulated by the relative filament length $L/(\pi R)$ and Coulomb interaction strength $\chi = \lambda^2 R/(4\pi\varepsilon_0\varepsilon_r\kappa)$. Based on point group symmetry, the system morphologies at different $(L/(\pi R), \chi)$ values fall into four symmetry groups: $D_{\infty h}$, D_2, C_{2h}, and C_i. For small values of $(L/(\pi R), \chi)$ (e.g., morphology at (1,0.4) in Fig. 2a), weak repulsion between the charged filaments results in minimal vesicle deformation, with only slight stretching due to weak pushing forces on the inner membrane. As χ increases, the vesicle transitions from an axisymmetric convex to a concave morphology (e.g., from (1,3) to (1,30) in Fig. 2a). Increasing $L/(\pi R)$ leads to lateral inflation and vertical shortening (comparing morphologies at (1,0.4) and (5/3,0.4)). MD simulations (Fig. 2b) yield morphologies consistent with numerical results.

With a further increase in $L/(\pi R)$, the compressive forces exerted by the vesicle membrane on the filaments intensify, destabilizing their position and morphology and triggering a system-wide transition. At small χ, axisymmetric morphologies with inversion symmetry $D_{\infty h}$ transform into those with D_2 symmetry (e.g., morphologies at (2,2) and (7/3,2) in Fig. 2a). At high χ, these $D_{\infty h}$ morphologies change into C_{2h} (e.g., morphology at (4/3,15)). The D_2 symmetry lacks mirror planes but features three twofold rotation axes, and C_{2h} has a twofold axis of rotation and a reflection plane. Regarding the filament loops as hand contours, the long, flexible filaments in D_2 system resemble a palm-to-palm handholding configuration with curled fingers. Increasing χ, the inter- and intrafilament interactions strengthen, repelling and straightening the saddle-shaped filaments. This drives the transition

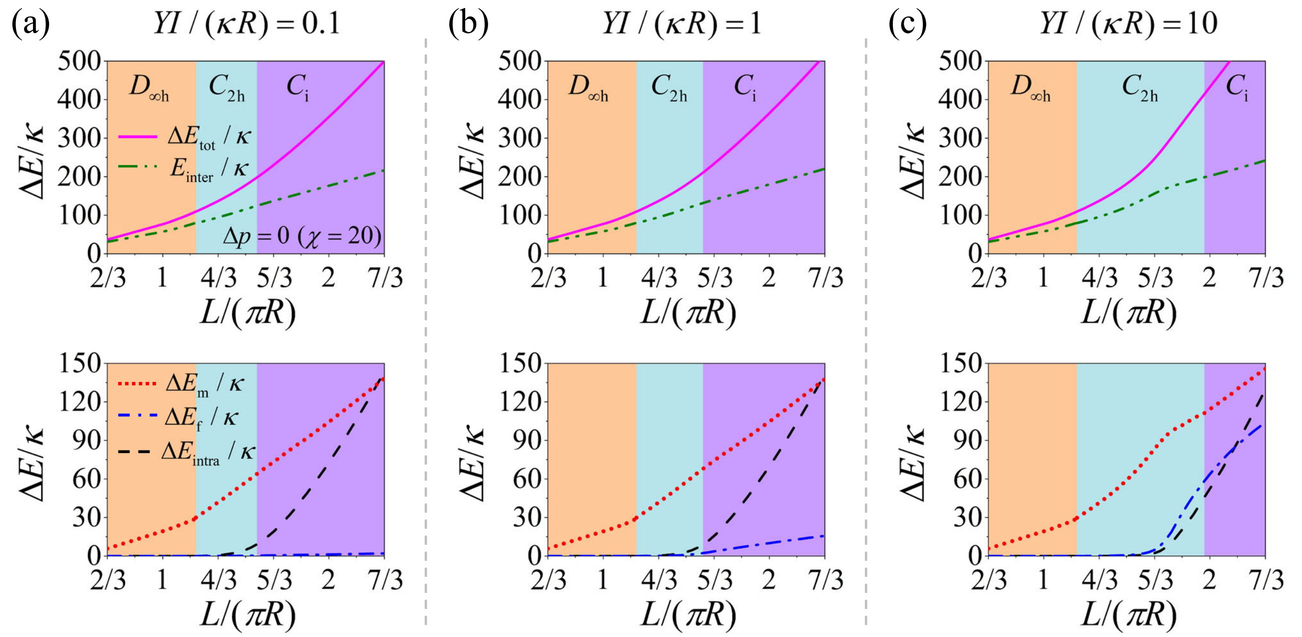

Fig. 3 | System energy profiles at $\Delta p = 0$ and $\chi = 20$. **a**–**c** show the total energy change ΔE_{tot} and its components ΔE_m, ΔE_f, ΔE_{intra}, and E_{inter} for relative filament stiffness values of $YI/(\kappa R) = 0.1$, 1, and 10, respectively.

from D_2 to C_i symmetry (e.g., morphology at (2,10)), where the vesicle adopts a rodlike shape with inversion as its sole symmetry element besides the identity. For the D_2 symmetry system at large $L/(\pi R)$ and small χ, the highly flexible filaments with $YI/(\kappa R) = 0.1$ minimally deform the vesicle, and their configurations approximate perturbed spherical curves (Supplementary Figs. S5 and S6)[33,34]. For $YI/(\kappa R) = 1$ and 10, representative system morphologies are presented in Supplementary Figs. S7 and S8, respectively.

With knowledge of all possible system morphologies at $\Delta p = 0$, we construct the corresponding morphological phase diagrams in Fig. 2c–e as functions of the relative filament length $L/(\pi R)$ and Coulomb interaction strength χ. The morphological transitions at $YI/(\kappa R) = 0.1$ and 1 exhibit qualitative similarity but differ quantitatively. One difference is that in the $D_{\infty h}$ and D_2 phases, with relatively large $L/(\pi R)$ and small χ, stiffer filaments deform the vesicle into an oblate shape (Supplementary Fig. S7a), whereas highly flexible filaments induce only minor deviations from a spherical morphology (Fig. 2a). Additionally, increasing $YI/(\kappa R)$ from 0.1 to 1 expands the $D_{\infty h}$ region, shifts the D_2 region rightward, and moves the C_{2h} region upward at large $L/(\pi R)$, consistent with the increased resistance of stiffer loops to buckling at longer critical lengths. At $YI/(\kappa R) = 10$, these trends intensify: the $D_{\infty h}$ region further expands, the D_2, C_{2h}, and C_i regions shift rightward and upward, respectively, and the D_2 phase disappears entirely within the studied $L/(\pi R) - \chi$ region (Fig. 2e).

To elucidate the mechanisms underlying the morphological phase transitions, the total energy change and its components are analyzed in Fig. 3. In the $\Delta p = 0$ case, the ground energy state consists of a spherical vesicle with bending energy $8\pi\kappa$ and two infinitely separated circular charged filaments, each of length L and charge density λ. The total energy change is $\Delta E_{tot} = \Delta E_m + \Delta E_f + \Delta E_{intra} + E_{inter}$, where $\Delta E_m = E_m - 8\pi\kappa$, $\Delta E_f = E_f - 4\pi^2 YI/L$, and $\Delta E_{intra} = E_{intra} - 1.029\pi\kappa\chi L/R$. Energy profiles at $\chi = 20$ (Fig. 3) show that the interfilament interaction energy E_{inter} dominates ΔE_{tot} throughout the vesicle evolution. As $L/(\pi R)$ increases, ΔE_{tot} exhibits a kink, marking a discontinuous morphological transition. In the transition from $D_{\infty h}$ (orange) to the C_{2h} phase (cyan), the filaments reorient and undergo significant in-plane bending, stretching the vesicle and sharply increasing both ΔE_m and ΔE_f. The transition from the C_{2h} to the C_i phase (purple) is continuous. With increasing filament bending stiffness, the energy contribution from filament bending grows. In the C_{2h} and C_i phases, ΔE_f plays a minor role at $YI/(\kappa R) = 0.1$ and 1 (Fig. 3a, b) but becomes comparable to ΔE_m and ΔE_{intra} at $YI/(\kappa R) = 10$ (Fig. 3c).

The morphological transition can also be understood from the evolution of the membrane tension. As χ increases, the growing interfilament repulsion stretches the confining vesicle, raising membrane tension σ (Fig. 4). This increased tension σ enhances radial contraction of the elongated vesicle. When the resulting distributed compressive force on the filaments becomes sufficiently large, they destabilize, undergoing rotation and bending, which drives the system's morphological transitions.

While this general mechanism applies across a range of parameters, the specific evolution of the membrane tension during the transition depends on the filament stiffness. For example, although both cases with $YI/(\kappa R) = 1$ and 10 undergo a similar morphological transition from an oblate axisymmetric shape ($D_{\infty h}$) to a centrosymmetric elongated shape (C_{2h}) with a central neck, the associated membrane tension exhibits opposite sharp changes: it drops for flexible filaments but jumps for stiff ones. This contrast arises from how filament stiffness modulates the geometric and mechanical constraints on the vesicle.

In systems with flexible filaments, the C_{2h} configuration allows the filaments to deform and adapt more easily, thereby exerting weaker geometric and mechanical constraints on the vesicle. This flexibility leads to a lower membrane tension compared to the case with stiff filaments, which resist deformation and act as stronger internal constraints. As a result, the vesicle must accommodate these stiff structures by increasing its membrane tension, even when the overall morphology appears similar, as confirmed in Supplementary Fig. S9.

Supplementary Fig. S9 further indicates that at low filament stiffness, the vesicle membrane tension is lower than that of the corresponding oblate axisymmetric state. As $YI/(\kappa R)$ increases, the tension surpasses that of the axisymmetric configuration and eventually saturates at a plateau. This behavior explains the sharp drop observed at $YI/(\kappa R) = 1$ and the jump at $YI/(\kappa R) = 10$ in the σ–χ profiles (Fig. 4).

Interacting filaments–vesicle system at a given vesicle volume

In preceding cases, the vesicles at $\Delta p = 0$ provide an isotropic confinement for the filaments. Here, we investigate how the mechanical

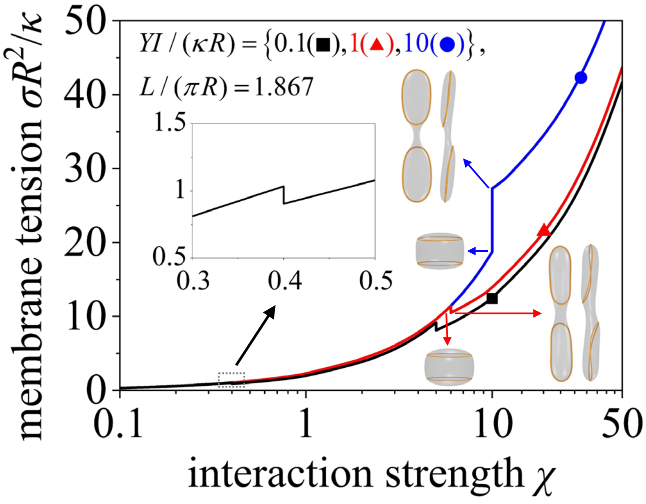

Fig. 4 | Membrane tension σ versus Coulomb interaction strength χ. The σ–χ profiles are evaluated at $\Delta p = 0$ and $L/(\pi R) = 1.867$ for $YI/(\kappa R) = 0.1$, 1, and 10. The tension $\sigma(= -\partial E_{\mathrm{tot}}/\partial A)$ is a Lagrange multiplier conjugated to the vesicle area A. Sharp drops and jumps in the σ–χ profiles mark discontinuous morphological transitions, with morphologies before and after transitions illustrated by arrows.

interplay between the charged filaments and the vesicle is influenced by a nonspherical, anisotropic confinement, achieved by specifying a reduced vesicle volume at $\upsilon = 0.9$ for example.

Figure 5a, b shows representative system morphologies for highly flexible filaments ($YI/(\kappa R) = 0.1$) at $\upsilon = 0.9$, and the corresponding morphological phase diagram is established in Fig. 5c. The system morphologies at different ($L/(\pi R)$, χ) values are categorized into symmetry groups: $D_{\infty h}$, C_{2h}, D_{2h}, and D_2, where D_{2h} symmetry has three mutually perpendicular reflection planes and an inversion center. At small $L/(\pi R)$, the filaments arranged in circular configurations with axisymmetric prolate vesicles ($D_{\infty h}$ symmetry), which transition from convex at smaller $L/(\pi R)$ (e.g., morphologies at (1,1) and (1,10) in Fig. 5a) to concave shapes at larger $L/(\pi R)$ (e.g., morphology at (11/8,1)). Increasing Coulomb interaction strength χ leads to progressive elongation of the axisymmetric vesicles.

As in the $\Delta p = 0$ case, increasing $L/(\pi R)$ further destabilizes filament loops, driving system transitions from $D_{\infty h}$ to C_{2h} and D_2 morphologies. However, a key difference at $\upsilon = 0.9$ is that C_{2h} morphologies appear at small χ, while D_2 morphologies emerge at large χ (Fig. 5c). This difference arises from the anisotropic confinement provided by the prolate vesicle, which naturally offers the filament loops suitable inclined positions to form the C_{2h} morphologies (e.g., morphology at (1.6,1) in Fig. 5a), eliminating the need for high χ, whereas the round vesicles at $\Delta p = 0$ require elongation (induced by stronger interfilament repulsion at high χ) to accommodate the inclined loops. The $D_{\infty h}$-to-C_{2h} transition is discontinuous, evidenced by abrupt filament sliding and reorientation (e.g., morphologies at (11/8,1) and (1.6,1)). Morphologies from MD simulations closely match those from numerical optimization (Fig. 5b).

The D_2 system morphologies, where the filaments resemble a palm-to-palm handholding configuration, are energetically preferred by round vesicles. For prolate vesicles at $\upsilon = 0.9$, achieving this state requires longer filament loops and higher χ to induce a more spherical geometry. This translates to expanded lateral dimensions and a reduced vertical dimension for the prolate vesicle (e.g., morphologies at (5/3,10) and (2.033,40) in Fig. 5a). Consequently, the $D_{\infty h}$-to-D_2 transition occurs at larger values of ($L/(\pi R)$, χ), compared to the $D_{\infty h}$-to-C_{2h} transition (Fig. 5c).

For the C_{2h} morphologies, a further increase in $L/(\pi R)$ leads to a transition to D_2 at high χ (e.g., morphology at (2.267,10) in Fig. 5a), and to D_{2h}, then D_2, at small χ (e.g., morphologies at (2.1,1) and (2.267,1)), with longer loops exhibiting greater bending. In D_{2h} morphologies, the filaments elongate and reorient parallel to the vesicle's long axis. Unlike other discontinuous transitions (solid phase boundaries in Fig. 5c), the C_{2h}-to-D_{2h} transition is continuous (dashed phase boundary).

Comparing phase diagrams at $YI/(\kappa R) = 1$ and 10 in Fig. 5d, e with that at $YI/(\kappa R) = 0.1$ in Fig. 5c, structural changes in morphology emerge as $YI/(\kappa R)$ increases. In D_{2h} and D_2 morphologies, the filament loops experience significant in-plane or out-of-plane bending (Supplementary Figs. S10 and S11). As $YI/(\kappa R)$ increases, this bending instability necessitates larger $L/(\pi R)$ and χ, shifting the D_{2h} and D_2 regions toward the upper right. The gaps between C_{2h} and D_{2h}, as well as between C_{2h} and D_2, are occupied by the $D_{\infty h}$ phase (Fig. 5d, e), where the filament loops remain circular. Further morphological results indicate that, for $YI/(\kappa R) = 1$ and 10 (Fig. 5d, e), the left $D_{\infty h}$-to-C_{2h} transition is discontinuous, marked by abrupt filament sliding and reorientation, whereas the right C_{2h}-to-$D_{\infty h}$ transition is continuous, exhibiting smooth filament rearrangement (Supplementary Figs. S10 and S11).

The energy analysis at $\upsilon = 0.9$ is given in Supplementary Fig. S12. Here, the ground state comprises a prolate vesicle with bending energy 29.90κ[32] and two circular, charged filaments (length L, charge density λ), positioned at infinite separation. Consequently, the changes in energy are $\Delta E_{\mathrm{m}} = E_{\mathrm{m}} - 29.90\kappa$, $\Delta E_{\mathrm{f}} = E_{\mathrm{f}} - 4\pi^2 YI/L$, and $\Delta E_{\mathrm{intra}} = E_{\mathrm{intra}} - 1.029\pi\kappa\chi L/R$. The energy profiles at $\chi = 1$ in Supplementary Fig. S12 indicate that the interfilament interaction energy E_{inter} dominates the total energy evolution, similar to the $\Delta p = 0$ case. For small values of ($L/(\pi R)$, χ), the filaments in circular configurations are far apart, resulting in negligible $\Delta E_{\mathrm{intra}}$. With increasing $L/(\pi R)$, the reorienting filaments undergo pronounced in-plane and out-of-plane bending, which raises ΔE_{f}. In the D_2 phase (green), the two approaching filaments bend more severely, causing substantial increases in both $\Delta E_{\mathrm{intra}}$ and ΔE_{f}. For filaments with $YI/(\kappa R) = 1$ and 10 (Supplementary Fig. S12b, c), ΔE_{f} remains minor relative to ΔE_{m} in the C_{2h} region (cyan), reflecting only slight filament deformation.

For a filament-free vesicle of $\upsilon = 0.9$, the membrane tension is $\sigma R^2/\kappa \approx -5.11$. The presence of repelling filaments increases σ as the vesicle is stretched. Fig. 6 shows the evolution of the membrane tension σ with the relative filament length $L/(\pi R)$ for different filament stiffnesses at $\chi = 1$ and 3. Positive (negative) σ means in-plane membrane tension (compression). Several sharp jumps and drops in σ mark discontinuous phase transitions.

Packing of inhomogeneous filament loops

Filaments within cells can experience localized mechanical property changes due to the influence of specific proteins[35]. For instance, cofilin-decorated filaments are more flexible than native filaments, and in some cases, cofilin molecules can induce filament breakage[36], whereas tropomyosin-troponin complexes increase the bending stiffness of actin filaments by stabilizing the filament structure[37]. To explore how filament inhomogeneity affects system morphologies, we consider two identical inhomogeneous filaments confined within a vesicle, each composed of flexible (s1) and stiffer (s2) segments (Fig. 7).

Figure 7 shows the system morphologies at $\Delta p = 0$ and $\upsilon = 0.9$ for a given filament interaction strength. At $\Delta p = 0$, the filaments have $Y_{s1}I_{s1}/(\kappa R) = 0.1$, $Y_{s2}I_{s2}/(\kappa R) = 1$, and segment lengths $L_{s1} = L_{s2} = 0.95\pi R$ at $\chi = 1$. As shown in Fig. 7a, they resemble a palm-to-palm arrangement with an approximate 90° relative orientation. At $\upsilon = 0.9$, filaments with $Y_{s1}I_{s1}/(\kappa R) = 1$, $Y_{s2}I_{s2}/(\kappa R) = 10$, and $L_{s1} = L_{s2} = 7\pi R/6$ at $\chi = 1$ exhibit nearly identical orientations (Fig. 7b), with stiffer segments aligned with each other and softer segments similarly positioned. In both cases, the filament deformation localizes at the ends of the relatively flexible segment (light brown or blue) to minimize the energy cost associated with bending the stiffer segment.

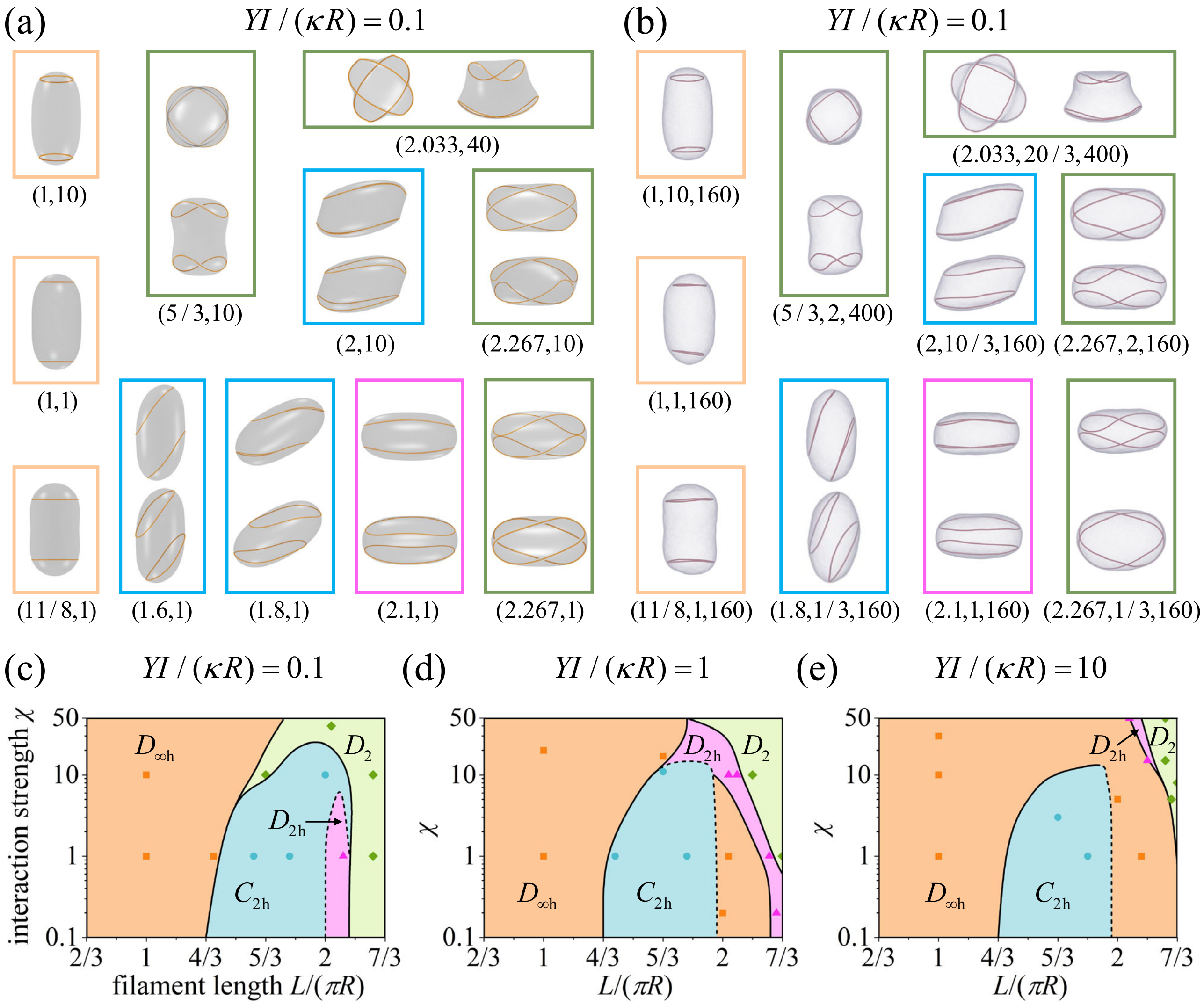

Fig. 5 | The interacting filaments–vesicle system at a reduced vesicle volume $\upsilon = 0.9$. Representative equilibrium system morphologies for highly flexible filaments ($YI/(\kappa R) = 0.1$) from numerical optimization (**a**) and MD simulations (**b**). **c**–**e** Morphological phase diagrams in terms of $L/(\pi R)$ and χ for $YI/(\kappa R) = 0.1$, 1, and 10, respectively. In **a**, $(L/(\pi R), \chi)$ values are provided below each morphology, while in (**b**), corresponding values of $(L/(\pi R), 1/\varepsilon_r, b_s/\Sigma)$ are given. The length scales in (**a**) and (**b**) are identical. The filament interaction strength in the MD simulations increases as ε_r decreases. Symbols in **c**–**e** correspond to the framed morphologies in (**a**), Supplementary Figs. S10, and Fig. S11. The solid (dashed) phase boundaries denote discontinuous (continuous) morphological transitions.

Discussion

The phase diagrams in Figs. 2c–e and 5c–e provide a robust quantitative framework for the rational design of artificial cellular architectures. This mechanical roadmap facilitates the systematic selection of filament-vesicle combinations by considering intrinsic material properties, biochemical modulation strategies, and functional integration. For instance, the distinct mechanical roles of cytoskeletal filaments suggest diverse architectural possibilities. Actin filaments, with their semi-flexible persistence lengths, enable adaptive membrane remodeling through buckling and branch reorganization, whereas stiffer microtubule assemblies could serve as anchoring structures to stabilize elongated vesicles. Biochemical strategies—such as cation-induced actin polymerization or protein-mediated modulation of filament stiffness[35]—can be synergistically combined with membrane-modifying agents (e.g., cholesterol, sphingomyelin, or unsaturated phospholipids) to establish hierarchical stiffness profiles. Moreover, emerging functionalization techniques that involve encapsulating responsive or active filaments within vesicles enable directional deformability.

With the advent of networks composed of programmed vesicles[38,39], it is now possible to fabricate vesicular machines with controlled, reversible folding for targeted transport, drug release, and mobility[40,41]. Under high interaction strength χ and long filament length L, the vesicles containing stiff interacting filament loops elongate more than those with flexible filaments. This deformation feature can be exploited to construct two-layer vesicle structures, wherein one layer comprises vesicle aggregates with flexible filament loops and the other with stiffer filaments. Under high-χ stimuli, these bilayer structures bend and subsequently recover as χ decreases, thereby facilitating gripping, release, and directional transport. Integrating living cells or organelles with artificial cells could further expand biohybrid system applications.

Throughout the main text, we adopt a salt-free environment as the baseline model, in which electrostatic interactions remain effectively unscreened. This idealized setting allows us to isolate the conceptual role of nonlocal repulsion without the complexity introduced by ionic screening. To assess the robustness of our findings under more realistic ionic conditions, we extend our model to incorporate electrostatic screening using a screened Coulomb potential with an adjustable Debye length λ_D[24,42]. The Debye length quantifies the range over which electrostatic interactions remain significant; a larger λ_D corresponds to weaker screening and thus longer-ranged interactions. As detailed in Supplementary Fig. S13 and corresponding supplementary discussion, simulations performed at varying λ_D reveal that, under weak screening conditions (e.g., $\lambda_D = 10$), filaments-vesicle morphologies remain qualitatively similar to the unscreened cases, indicating that the morphological transitions are robust against mild ionic attenuation. Under strong screening (e.g., $\lambda_D = 0.1$), the effective filament repulsion is substantially reduced, leading to a downward shift of the phase boundary and requiring stronger interaction strength to achieve comparable morphological transitions. These results quantitatively demonstrate how screening modulates long-range interactions and confirm that such interactions effectively drive morphological transitions of the system.

A key step toward experimentally realizing the morphologies predicted in our model is the construction of microscale filaments that actively respond to external stimuli such as magnetic fields, electric fields, or light. Recent advances in soft matter and nanomanufacturing offer promising strategies for building such reconfigurable and stimulus-responsive filaments with tunable mechanics. For instance, Bharti et al. demonstrated the magnetic assembly of ultraflexible microfilaments composed of lipid-coated magnetic nanoparticles held together by nanocapillary forces[43]. These filaments exhibit exceptional flexibility, reversibility, and the ability to self-close into loops or figure-eight configurations under external magnetic fields. Beyond self-assembly, other fabrication approaches include embedding superparamagnetic nanoparticles into electrospun or wet-spun polymer nanofibers, and incorporating photoresponsive moieties, gold nanorods, or liquid crystal droplets into filament backbones using techniques such as coaxial electrospinning or direct ink writing. These methods allow for programmable filament stiffness, curvature adaptability, and responsiveness to environmental cues. Such capabilities make it feasible to design soft, reconfigurable filaments that recapitulate the confinement-driven shape transformations predicted by our theory.

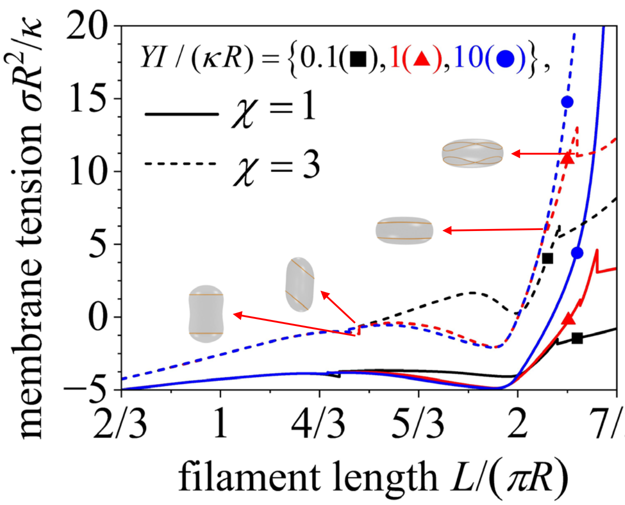

Fig. 6 | The vesicle membrane tension σ versus the relative filament length $L/(\pi R)$. The σ–$L/(\pi R)$ profiles for different filament stiffness values are evaluated at the interaction strengths $\chi = 1$ and 3, with a reduced volume $v = 0.9$.

To explore the magnetic field-based control of the filament interaction, we propose a system composed of one paramagnetic and one diamagnetic filament confined within a vesicle. When exposed to an external magnetic field, the paramagnetic filament acquires a magnetic moment aligned with the field, while the diamagnetic filament develops a moment in the opposite direction (Supplementary Fig. S14). This antiparallel dipole alignment induces a repulsive dipole–dipole interaction along the magnetic field axis. By incorporating the standard dipole–dipole interaction potential[44] into both inter- and intrafilament interactions, we reveal a spectrum of vesicle morphologies (Supplementary Fig. S15)—including elongation, flattening, and neck formation—that closely mirror those obtained in the electrostatic case. These results demonstrate that magnetic contrast between filaments can serve as a physically realizable surrogate for nonlocal repulsion. In this context, flexible paramagnetic chains assembled from superparamagnetic beads and diamagnetic filaments formed from carbon-based materials or polymer-coated colloids may provide a viable experimental platform for validating the theoretical predictions.

Although the specific system explored in this study has not yet been directly realized experimentally, our predictions show strong

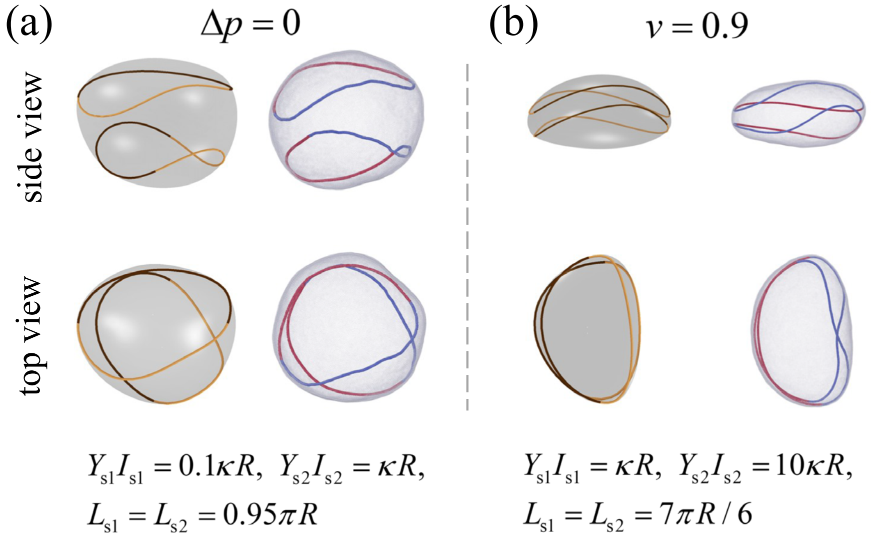

Fig. 7 | Vesicle morphologies with inhomogeneous filaments. Selected equilibrium morphologies obtained from numerical optimization (left panels) and MD simulations (right panels). Cases of $\Delta p = 0$ (**a**) and $v = 0.9$ (**b**). For the theoretical modeling, $\chi = 1$ is used. In the MD simulations, the simulation box size is $b_s = 160\Sigma$, and $1/\varepsilon_r = 0.351$ (**a**) and 0.333 (**b**). Each inhomogeneous filament has two segments, more flexible segment #1 (light brown or blue) of length L_{s1} and bending stiffness $Y_{s1}I_{s1}$ and stiffer segment #2 (dark brown or crimson) of length L_{s2} and bending stiffness $Y_{s2}I_{s2}$.

parallels with deformation observed in related biological and biomimetic systems. For example, during mitosis, forces generated by the mitotic spindle lead to elongation and necking of the nuclear envelope[45,46], resembling the vesicle morphologies induced by interacting filament loops in our model. Similarly, giant unilamellar vesicles subjected to extensional flow develop elongated and asymmetric morphologies due to flow-induced membrane tension[47,48]. In both cases, the membrane deformation is driven by internally generated forces (e.g., microtubule polymerization and sliding) or externally imposed hydrodynamic forces. These mechanisms are conceptually similar to the repulsive interactions produced by confined filament loops in our model.

Additional parallels can be drawn with endocytosis, which involves membrane shape transformations such as elongation, necking, and symmetry breaking that are qualitatively similar to those observed in our simulations. Membrane-associated filaments such as dynamin and endosomal sorting complexes required for transport (ESCRT-III) play central roles in driving these transitions. For instance, dynamin helices constrict membrane necks during vesicle scission events[49], while ESCRT-III filaments undergo supercoiling and reorganization to remodel membrane geometry[50]. These examples illustrate how filament-membrane coupling, whether driven actively or arising passively through geometric constraints, can produce complex shape transitions analogous to those captured in our mechanical model. Together, these biological analogies underscore the broader applicability of our framework and suggest that its underlying mechanical principles may be experimentally accessible using either biological analogs or synthetic reconstitution platforms.

Biological and synthetic systems also support the plausibility of ring-like filament structures. For example, Miyazaki et al. showed that polymerizing actin filaments confined within spherical droplets can spontaneously self-organize into equatorial rings driven by filament elasticity and confinement[8]. Similarly, experimental observations demonstrated that actin filaments cross-linked by proteins such as α-actinin and muscle filamin can form stable ring-like bundles within giant unilamellar vesicles under appropriate conditions[9]. Another relevant example is the marginal band in blood platelets, a peripheral ring of microtubules that provides internal mechanical support and undergoes buckling transitions during activation[6]. These examples illustrate that while the closed-loop geometry in our model is idealized, the underlying mechanisms—elastic confinement, curvature-induced organization, and topological coupling—are broadly realized in both synthetic and biological contexts.

In addition to spatial organization, the dynamical nature of filament-vesicle systems also merits consideration. While the present study focuses on equilibrium morphologies, many biological vesicle-filament systems exhibit dynamic remodeling driven by active processes such as filament polymerization, motor-protein forces, and ATP-dependent turnover[1]. Nonetheless, our results demonstrate that passive mechanical and physical interactions, specifically long-range filament repulsion and elasticity under confinement, are already sufficient to induce robust shape transformations, filament localization, and symmetry breaking. These phenomena mirror qualitative features commonly observed in active systems, suggesting that certain morphogenetic patterns may emerge purely from mechanical coupling, independent of nonequilibrium driving. From this perspective, our model provides a minimal mechanical framework that isolates the role of internal stress and offers a baseline for understanding more complex systems.

Recent studies have indeed shown that active cytoskeletal networks, such as microtubule-motor assemblies, can induce dynamic vesicle shape fluctuations through internally generated stresses[15]. These systems display pronounced time-dependent behaviors and fluctuation spectra characteristic of nonequilibrium dynamics. In contrast, our equilibrium-based model enables the controlled programming of stable vesicle morphologies through tunable filament interactions. Together, the active and equilibrium perspectives define a broader design space for vesicle-based systems, spanning from fluctuation-induced remodeling and dynamic reconfigurability to shape locking via filament-mediated mechanical feedback.

Building on this foundation, future extensions of our model could incorporate active components such as filament-length evolution, polymerization-driven remodeling, and motor-induced force generation. These additions would allow for the exploration of nonequilibrium shape fluctuations, remodeling pathways, and adaptive morphologies, thereby bridging equilibrium-based design principles with the spatiotemporal complexity of living systems.

In summary, this study reveals how enclosed interacting filament loops drive vesicle morphogenesis, with phase diagrams illustrating the influence of filament stiffness, length, and interaction strength on morphological transitions. For short filaments, increasing interaction strength transforms the vesicle from an axisymmetric convex to a concave shape. At higher filament lengths and interaction strengths, filament loops destabilize, leading to asymmetric morphologies characterized by in- and out-of-plane buckling and reorientation. In vesicles with specified relative volumes, geometric anisotropy alters the sequence of morphological phases compared to those at zero pressure. Energy analysis shows that interfilament interactions are the primary drivers of total energy changes. Our results provide a quantitative foundation for the rational design of artificial, programmable cellular systems and enhance our understanding of cell shaping and stability.

Methods

Numerical optimization

In the numerical optimization, the vesicle morphology is depicted by the membrane position vector $\mathbf{r}^{\mathrm{m}}$ using a spherical harmonic parameterization[21,51,52]. In a Cartesian coordinate system *Oxyz* (Fig. 1), coordinates of $\mathbf{r}^{\mathrm{m}} = (x^{\mathrm{m}}, y^{\mathrm{m}}, z^{\mathrm{m}})$ are $x^{\mathrm{m}} = \sum_{l=0}^{l_{\max}} \sum_{m=-l}^{l} C_{lm}^{x} y_{lm}(\theta, \varphi)$ ($l_{\max} = 5$ is taken) and similar forms for y^{m} and z^{m} by replacing C_{lm}^{x} with C_{lm}^{y} and C_{lm}^{z}, respectively. Here, $y_{lm}(\theta, \varphi)$ denotes the real spherical harmonic basis function in terms of the polar angle $\theta \in [0, \pi]$ and azimuthal angle $\varphi \in [0, 2\pi]$ of the spherical coordinate system (see Supplementary Note 1). The charged filaments, which repel each other, bend against the vesicle membrane and are assumed to be constrained to the membrane surface in our theoretical model, consistent with qualitative suggestions from MD simulations. The filaments could freely slip along the vesicle surface. Each filament f_i ($i = 1, 2$) is characterized by its position vector $\mathbf{r}_i^{\mathrm{f}}(\varphi) = \mathbf{r}^{\mathrm{m}}(\theta_i, \varphi)$, with a specified polar angle θ_i. The vesicle surface and filament geometries can then be derived from $\mathbf{r}^{\mathrm{m}}(\theta, \varphi)$ and $\mathbf{r}_i^{\mathrm{f}}(\varphi)$ using classical differential geometry (Supplementary Note 1). Consequently, the total energy E_{tot} is expressed as a function of undetermined coefficients $C_{lm}^{x,y,z}$ and minimized numerically via sequential quadratic programming. The fixed vesicle area A and filament length L_i serve as equality constraints, with vesicle volume V included if a reduced volume is specified. Once values of $C_{lm}^{x,y,z}$ are obtained, the system morphology and corresponding energy components are determined.

MD simulations

In the coarse-grained MD simulations, the lipid vesicle membrane is represented by a one-particle-thick layer[53–55], where each lipid molecule is modeled as a particle with translational and rotational degrees of freedom. The interaction between these lipid particles depends on their relative distances and orientations. For vesicles at $\Delta p = 0$, solvent is not introduced; for vesicles with a reduced volume υ, solvent is included to control volume[56]. Filaments are modeled as chains of unit-charged particles connected by harmonic bonds and angles. The electrostatic interaction is computed using the Particle-Particle Particle-Mesh method[57] with the interaction strength proportional to $1/\varepsilon_{\mathrm{r}}$.

The discretization of charges, finite simulation box size, and periodic boundary conditions complicate the mapping of the interaction strength from MD simulations to the theoretical model[58]. Lennard-Jones potentials govern lipid, solvent, and filament interactions[54]. For elongated vesicle morphologies at $\Delta p = 0$, the simulation box size b_s is adjusted to adequately accommodate the morphologies. All MD simulations are conducted with the Large-scale Atomic/Molecular Massively Parallel Simulator (LAMMPS)[59] and visualized using OVITO[60]. For clarity, simulation boxes and solvent particles are not shown in the main text. More detailed descriptions can be found in Supplementary Note 2 and Figs. S1–S4.

Reporting summary

Further information on research design is available in the Nature Portfolio Reporting Summary linked to this article.

Data availability

Simulation data generated in this study have been deposited in the PKU NetDisk database under accession code https://disk.pku.edu.cn/link/AA4B4C4DFE38E34C05B6A5C8CF0564813B.

References

1. Bray, D. *Cell Movements: From Molecules to Motility* 2nd edn (Garland Science, New York, 2001).
2. Litschel, T. & Schwille, P. Protein reconstitution inside giant unilamellar vesicles. *Annu. Rev. Biophys.* **50**, 525–548 (2021).
3. Lipowsky, R. (ed) *Multiresponsive Behavior of Biomembranes and Giant Vesicles. Advances in Biomembranes and Lipid Self-Assembly*, Vol. 30 (Academic Press, London, 2019).
4. Dimova, R. & Marques, C. (eds) *The Giant Vesicle Book* (CRC Press, Boca Raton, 2019).
5. Ramesh, S. & Kulkarni, Y. Statistical mechanics of active vesicles and the size distribution paradox. *J. Mech. Phys. Solids* **191**, 105749 (2024).
6. Diagouraga, B. et al. Motor-driven marginal band coiling promotes cell shape change during platelet activation. *J. Cell Biol.* **204**, 177–185 (2014).
7. Zhu, W. et al. Nanomechanical mechanism for lipid bilayer damage induced by carbon nanotubes confined in intracellular vesicles. *Proc. Natl. Acad. Sci. USA* **113**, 12374–12379 (2016).
8. Miyazaki, M., Chiba, M., Eguchi, H., Ohki, T. & Ishiwata, S. Cell-sized spherical confinement induces the spontaneous formation of contractile actomyosin rings in vitro. *Nat. Cell Biol.* **17**, 480–489 (2015).
9. Limozin, L. & Sackmann, E. Polymorphism of cross-linked actin networks in giant vesicles. *Phys. Rev. Lett.* **89**, 168103 (2002).
10. Mulla, Y., Aufderhorst-Roberts, A. & Koenderink, G. H. Shaping up synthetic cells. *Phys. Biol.* **15**, 041001 (2018).
11. Bashirzadeh, Y. & Liu, A. P. Encapsulation of the cytoskeleton: towards mimicking the mechanics of a cell. *Soft Matter* **15**, 8425–8436 (2019).
12. Litschel, T. et al. Reconstitution of contractile actomyosin rings in vesicles. *Nat. Commun.* **12**, 2254 (2021).
13. Baldauf, L., van Buren, L., Fanalista, F. & Koenderink, G. H. Actomyosin-driven division of a synthetic cell. *ACS Synth. Biol.* **11**, 3120–3133 (2022).
14. Graham, K. et al. Liquid-like VASP condensates drive actin polymerization and dynamic bundling. *Nat. Phys.* **19**, 574–585 (2023).
15. Sciortino, A. et al. Active membrane deformations of a minimal synthetic cell. *Nat. Phys.* **21**, 799–807 (2025).
16. Takatori, S. C. & Sahu, A. Active contact forces drive nonequilibrium fluctuations in membrane vesicles. *Phys. Rev. Lett.* **124**, 158102 (2020).
17. Abaurrea-Velasco, C., Auth, T. & Gompper, G. Vesicles with internal active filaments: self-organized propulsion controls shape, motility, and dynamical response. *New J. Phys.* **21**, 123024 (2019).
18. Peterson, M. S. E., Baskaran, A. & Hagan, M. F. Vesicle shape transformations driven by confined active filaments. *Nat. Commun.* **12**, 7247 (2021).
19. Iyer, P., Gompper, G. & Fedosov, D. A. Non-equilibrium shapes and dynamics of active vesicles. *Soft Matter* **18**, 6868–6881 (2022).
20. Shi, X.-Q. & Ma, Y.-Q. Topological structure dynamics revealing collective evolution in active nematics. *Nat. Commun.* **4**, 3013 (2013).
21. Shi, C. et al. Morphological transformations of vesicles with confined flexible filaments. *Proc. Natl. Acad. Sci. USA* **120**, e2300380120 (2023).
22. Behera, A., Kumar, G. & Sain, A. Confined filaments in soft vesicles–the case of sickle red blood cells. *Soft Matter* **16**, 421–427 (2020).
23. Zou, G., Yi, X., Zhu, W. & Gao, H. Packing of flexible nanofibers in vesicles. *Extreme Mech. Lett.* **19**, 20–26 (2018).
24. Dobrynin, A. V. & Rubinstein, M. Theory of polyelectrolytes in solutions and at surfaces. *Prog. Polym. Sci.* **30**, 1049–1118 (2005).
25. Maleki, M. & Fried, E. Stability of discoidal high-density lipoprotein particles. *Soft Matter* **9**, 9991–9998 (2013).
26. Belyi, V. A. & Muthukumar, M. Electrostatic origin of the genome packing in viruses. *Proc. Natl. Acad. Sci. USA* **103**, 17174–17178 (2006).
27. Purohit, P. K., Kondev, J. & Phillips, R. Mechanics of DNA packaging in viruses. *Proc. Natl. Acad. Sci. USA* **100**, 3173–3178 (2003).
28. Helfrich, W. Elastic properties of lipid bilayers: theory and possible experiments. *Z. Naturforsch. C* **28**, 693–703 (1973).
29. Doi, M. & Edwards, S.F. *The Theory of Polymer Dynamics* (Oxford Univ. Press, New York, 1986).
30. Hoffman, K. A. & Manning, R. S. An extended conjugate point theory with application to the stability of planar buckling of an elastic rod subject to a repulsive self-potential. *SIAM J. Math. Anal.* **41**, 465–494 (2009).
31. Chaurasia, V., Chen, Y.-C. & Fried, E. Interacting charged elastic loops on a sphere. *J. Mech. Phys. Solids* **134**, 103771 (2020).
32. Seifert, U., Berndl, K. & Lipowsky, R. Shape transformations of vesicles: phase diagram for spontaneous-curvature and bilayer-coupling models. *Phys. Rev. A* **44**, 1182 (1991).
33. Alben, S. Packings of a charged line on a sphere. *Phys. Rev. E* **78**, 066603 (2008).
34. Wang, M., Li, X. & Yi, X. Deformation, shape transformations, and stability of elastic rod loops within spherical confinement. *J. Mech. Phys. Solids* **191**, 105771 (2024).
35. Blanchoin, L., Boujemaa-Paterski, R., Sykes, C. & Plastino, J. Actin dynamics, architecture, and mechanics in cell motility. *Physiol. Rev.* **94**, 235–263 (2014).
36. McCullough, B. R., Blanchoin, L., Martiel, J.-L. & Enrique, M. Cofilin increases the bending flexibility of actin filaments: implications for severing and cell mechanics. *J. Mol. Biol.* **381**, 550–558 (2008).
37. Goldmann, W. H. Binding of tropomyosin–troponin to actin increases filament bending stiffness. *Biochem. Biophys. Res. Commun.* **276**, 1225–1228 (2000).
38. Bolognesi, G. et al. Sculpting and fusing biomimetic vesicle networks using optical tweezers. *Nat. Commun.* **9**, 1882 (2018).
39. Li, Q., Li, S., Zhang, X., Xu, W. & Han, X. Programmed magnetic manipulation of vesicles into spatially coded prototissue architectures arrays. *Nat. Commun.* **11**, 232 (2020).
40. Lipowsky, R. From membranes to membrane machines. in *Statistical Mechanics of Biocomplexity*, Vol. 527 (eds Reguera, D., Vilar, J. & Rubi, J.) (Springer, Berlin, Heidelberg, 1999).
41. Abdelmohsen, L. K. E. A. et al. Dynamic loading and unloading of proteins in polymeric stomatocytes: formation of an enzyme-loaded supramolecular nanomotor. *ACS Nano* **10**, 2652–2660 (2016).

42. Muthukumar, M. Adsorption of a polyelectrolyte chain to a charged surface. *J. Chem. Phys.* **86**, 7230–7235 (1987).
43. Bharti, B., Fameau, A.-L., Rubinstein, M. & Velev, O. D. Nanocapillarity-mediated magnetic assembly of nanoparticles into ultraflexible filaments and reconfigurable networks. *Nat. Mater.* **14**, 1104–1109 (2015).
44. Sano, T. G. Reduced theory for hard magnetic rods with dipole–dipole interactions. *J. Phys. A Math. Theor.* **55**, 104002 (2022).
45. Yam, C., He, Y., Zhang, D., Chiam, K.-H. & Oliferenko, S. Divergent strategies for controlling the nuclear membrane satisfy geometric constraints during nuclear division. *Curr. Biol.* **21**, 1314–1319 (2011).
46. Dey, G. et al. Closed mitosis requires local disassembly of the nuclear envelope. *Nature* **585**, 119–123 (2020).
47. Kantsler, V., Segre, E. & Steinberg, V. Vesicle dynamics in time-dependent elongation flow: Wrinkling instability. *Phys. Rev. Lett.* **99**, 178102 (2007).
48. Kantsler, V., Segre, E. & Steinberg, V. Critical dynamics of vesicle stretching transition in elongational flow. *Phys. Rev. Lett.* **101**, 048101 (2008).
49. Ganichkina, O. M. et al. Quantification and demonstration of the collective constriction-by-ratchet mechanism in the dynamin molecular motor. *Proc. Natl. Acad. Sci. USA* **118**, e2101144118 (2021).
50. Meadowcroft, B. & Palaja, I. et al. Mechanochemical rules for shape-shifting filaments that remodel membranes. *Phys. Rev. Lett.* **129**, 268101 (2022).
51. Khairy, K. & Howard, J. Minimum-energy vesicle and cell shapes calculated using spherical harmonics parameterization. *Soft Matter* **7**, 2138–2143 (2011).
52. Zhang, C., Fang, Y., Shi, C., Yuan, H. & Yi, X. Stretching transition of vesicles with confined filament loops: Morphological evolution with filament distortion and reorientation. *Giant* **17**, 100233 (2024).
53. Yuan, H., Huang, C., Li, J., Lykotrafitis, G. & Zhang, S. One-particle-thick, solvent-free, coarse-grained model for biological and biomimetic fluid membranes. *Phys. Rev. E* **82**, 011905 (2010).
54. Fu, S.-P., Peng, Z., Yuan, H., Kfoury, R. & Young, Y.-N. Lennard-Jones type pair-potential method for coarse-grained lipid bilayer membrane simulations in LAMMPS. *Comput. Phys. Commun.* **210**, 193–203 (2017).
55. Liu, Y., Zou, G. & Gao, H. Domain aggregation and associated pore growth in lipid membranes. *ACS Nano* **15**, 604–613 (2021).
56. Ghosh, R., Satarifard, V., Grafmüller, A. & Lipowsky, R. Spherical nanovesicles transform into a multitude of nonspherical shapes. *Nano Lett.* **19**, 7703–7711 (2019).
57. Eastwood, J. W., Hockney, R. W. & Lawrence, D. N. P3M3DP–The three-dimensional periodic particle-particle/particle-mesh program. *Comput. Phys. Commun.* **19**, 215–261 (1980).
58. Yeh, I.-C. & Hummer, G. System-size dependence of diffusion coefficients and viscosities from molecular dynamics simulations with periodic boundary conditions. *J. Phys. Chem. B* **108**, 15873–15879 (2004).
59. Plimpton, S. Fast parallel algorithms for short-range molecular dynamics. *J. Comput. Phys.* **117**, 1–19 (1995).
60. Stukowski, A. Visualization and analysis of atomistic simulation data with OVITO–the Open Visualization Tool. *Model. Simul. Mater. Sci. Eng.* **18**, 015012 (2009).

Acknowledgements

This work was supported by the National Natural Science Foundation of China, grant numbers 12272004 (X.Y.) and T2488101 (H.G.). We also gratefully acknowledge the High-Performance Computing Platform of Peking University for computational resources.

Author contributions

X.Y. and H.G. designed and guided this work; C.Z., G.Z., Y.F., H.G., and X.Y. performed the modeling and simulations, analyzed the data, and wrote the paper.

Competing interests

The authors declare no competing interests.

Additional information

Supplementary information The online version contains supplementary material available at https://doi.org/10.1038/s41467-025-66750-4.

Correspondence and requests for materials should be addressed to Huajian Gao or Xin Yi.

Peer review information *Nature Communications* thanks Ming Li and the other, anonymous, reviewer(s) for their contribution to the peer review of this work. A peer review file is available.

Supplementary Information for "Interacting filaments drive vesicle morphogenesis"

Chengyao Zhang[1,3], Guijin Zou[2,3], Yaxin Fang[1], Huajian Gao[2]✉ & Xin Yi[1]✉

[1]School of Mechanics and Engineering Science, Peking University, Beijing, China.

[2]Mechano-X Institute, Tsinghua University, Beijing, China.

[3]These authors contributed equally: Chengyao Zhang, Guijin Zou.

✉e-mail: gao.huajian@tsinghua.edu.cn (H.G.); xyi@pku.edu.cn (X.Y.)

Note 1. Geometrical characterization of the vesicle and filament morphologies in modeling

In our theoretical modeling, we employ spherical harmonic parameterization to describe the vesicle morphology. The position vector $\mathbf{r}^{\mathrm{m}}$ of the vesicle membrane is given by

$$\mathbf{r}^{\mathrm{m}}(\theta,\varphi)=\begin{bmatrix} x^{\mathrm{m}}(\theta,\varphi) \\ y^{\mathrm{m}}(\theta,\varphi) \\ z^{\mathrm{m}}(\theta,\varphi) \end{bmatrix}=\begin{bmatrix} \sum_{l=0}^{l_{\max}}\sum_{m=-l}^{l} C_{lm}^{x} y_{lm}(\theta,\varphi) \\ \sum_{l=0}^{l_{\max}}\sum_{m=-l}^{l} C_{lm}^{y} y_{lm}(\theta,\varphi) \\ \sum_{l=0}^{l_{\max}}\sum_{m=-l}^{l} C_{lm}^{z} y_{lm}(\theta,\varphi) \end{bmatrix}.$$

Here, $\theta\in[0,\pi]$ and $\varphi\in[0,2\pi]$ denote the polar and azimuthal angles in the spherical coordinate system, respectively, and $y_{lm}(\theta,\varphi)$ is the real spherical harmonic basis function expressed as

$$y_{lm}(\theta,\varphi)=\begin{cases} \sqrt{2}N_{lm}P_{lm}(\cos\theta)\cos(m\varphi), & m>0, \\ N_{l0}P_{l0}(\cos\theta), & m=0, \\ \sqrt{2}N_{lm}P_{lm}(\cos\theta)\sin(-m\varphi), & m<0, \end{cases}$$

where

$$N_{lm}=\frac{1}{2}\sqrt{\frac{(2l+1)(l-|m|)!}{\pi(l+|m|)!}} \quad \text{and} \quad P_{lm}(X)=\frac{(-1)^{|m|}}{2^{l}l!}(1-X^{2})^{|m|/2}\frac{\mathrm{d}^{l+|m|}[(X^{2}-1)^{l}]}{\mathrm{d}X^{l+|m|}}.$$

Using the expression of $\mathbf{r}^{\mathrm{m}}(\theta,\varphi)$, geometrical properties of the vesicle such as surface area, volume, and local curvature are derived. Subsequently, the bending energy of the vesicle membrane is obtained using the Helfrich theory.

The surface area A and volume V of the vesicle are given by

$$A=\int_{0}^{2\pi}\int_{0}^{\pi}|\mathbf{r}_{,\theta}^{\mathrm{m}}\times\mathbf{r}_{,\varphi}^{\mathrm{m}}|\,\mathrm{d}\theta\mathrm{d}\varphi \quad \text{and} \quad V=\frac{1}{3}\int_{0}^{2\pi}\int_{0}^{\pi}\mathbf{r}^{\mathrm{m}}\cdot(\mathbf{r}_{,\theta}^{\mathrm{m}}\times\mathbf{r}_{,\varphi}^{\mathrm{m}})\mathrm{d}\theta\mathrm{d}\varphi,$$

respectively. Here, a subscript comma followed by a variable denotes partial differentiation with respect to that variable (e.g., $\mathbf{r}_{,\theta}^{\mathrm{m}}\equiv\partial\mathbf{r}^{\mathrm{m}}/\partial\theta$).

The local mean curvature H of the vesicle surface is

$$H=\frac{EN+GL-2FM}{2(EG-F^{2})},$$

where $E=\mathbf{r}^{\mathrm{m}}_{,\theta}\cdot\mathbf{r}^{\mathrm{m}}_{,\theta}$, $F=\mathbf{r}^{\mathrm{m}}_{,\theta}\cdot\mathbf{r}^{\mathrm{m}}_{,\varphi}$, and $G=\mathbf{r}^{\mathrm{m}}_{,\varphi}\cdot\mathbf{r}^{\mathrm{m}}_{,\varphi}$ are coefficients of the first fundamental form of the surface at the point $\mathbf{r}^{\mathrm{m}}$, and $L=\mathbf{r}^{\mathrm{m}}_{,\theta\theta}\cdot\mathbf{n}^{\mathrm{m}}$, $M=\mathbf{r}^{\mathrm{m}}_{,\theta\varphi}\cdot\mathbf{n}^{\mathrm{m}}$, and $N=\mathbf{r}^{\mathrm{m}}_{,\varphi\varphi}\cdot\mathbf{n}^{\mathrm{m}}$ are coefficients of the second fundamental form with $\mathbf{n}^{\mathrm{m}}=\mathbf{r}^{\mathrm{m}}_{,\theta}\times\mathbf{r}^{\mathrm{m}}_{,\varphi}/|\mathbf{r}^{\mathrm{m}}_{,\theta}\times\mathbf{r}^{\mathrm{m}}_{,\varphi}|$ as the unit normal vector of the surface.

The bending energy E_{m} of the vesicle membrane is

$$E_{\mathrm{m}}=2\kappa\int H^2\mathrm{d}A=2\kappa\int_0^{2\pi}\int_0^{\pi}H^2\sqrt{EG-F^2}\mathrm{d}\theta\mathrm{d}\varphi.$$

The morphology of each surface-constrained filament f_i (i = 1,2) is characterized by its position vector $\mathbf{r}_i^{\mathrm{f}}(\varphi)=\mathbf{r}^{\mathrm{m}}(\theta_i,\varphi)$, where θ_i is the specified polar angle. The length L_i of the filament f_i is

$$L_i=\int_0^{L_i}\mathrm{d}s_i=\int_0^{2\pi}|\mathbf{r}^{\mathrm{f}}_{i,\varphi}|\mathrm{d}\varphi.$$

The local curvature C_i of the filament f_i is given by

$$C_i=\frac{|\mathbf{r}^{\mathrm{f}}_{i,\varphi}\times\mathbf{r}^{\mathrm{f}}_{i,\varphi\varphi}|}{|\mathbf{r}^{\mathrm{f}}_{i,\varphi}|^3},$$

and the total bending energy of the filaments f_1 and f_2 is

$$E_{\mathrm{f}}=\sum_{i=1,2}\frac{Y_iI_i}{2}\int_0^{L_i}C_i^2\mathrm{d}s_i=\sum_{i=1,2}\frac{Y_iI_i}{2}\int_0^{2\pi}\frac{|\mathbf{r}^{\mathrm{f}}_{i,\varphi}\times\mathbf{r}^{\mathrm{f}}_{i,\varphi\varphi}|^2}{|\mathbf{r}^{\mathrm{f}}_{i,\varphi}|^5}\mathrm{d}\varphi.$$

If the filament f_i is inhomogeneous, consisting of two segments with different bending stiffnesses, the above integrals for L_i and E_{f} with respect to φ are evaluated over the intervals $[0,\varphi_j]$ and $[\varphi_j,2\pi]$, where φ_j is the specified azimuthal angle.

Note 2. Coarse-grained molecular dynamics (MD) simulations

Coarse-grained model of lipid membranes. We employ a one-particle-thick lipid membrane model [1-3] to simulate lipid membranes. This model represents each lipid molecule as a single spherical particle, which possesses both translational and rotational degrees of freedom (Fig. S1). The interactions between lipid particles depend on their relative distances and orientations. The potential energy between two lipid particles i and j is given by

$$U(\mathbf{r}_{ij},\mathbf{n}_i,\mathbf{n}_j)=\begin{cases}U_{\mathrm{R}}(r)+\varepsilon[1-\phi(\hat{\mathbf{r}}_{ij},\mathbf{n}_i,\mathbf{n}_j)], & r<r_{\mathrm{min}},\\ U_{\mathrm{A}}(r)\phi(\hat{\mathbf{r}}_{ij},\mathbf{n}_i,\mathbf{n}_j), & r_{\mathrm{min}}<r<r_{\mathrm{c}},\end{cases}$$

where r is the distance between lipid particles i and j, $U_{\mathrm{R}}(r)$ and $U_{\mathrm{A}}(r)$ represent the distance-dependent repulsive and attractive potentials, respectively. The parameter r_{min} denotes the range of the repulsive force, while r_{c} is the cutoff distance for pairwise interaction. The function $\phi(\hat{\mathbf{r}}_{ij},\mathbf{n}_i,\mathbf{n}_j)$ adjusts the interaction based on the relative orientation of particles i and j, with $\hat{\mathbf{r}}_{ij}=\mathbf{r}_{ij}/r$ serving as the direction vector of the relative distance vector $\mathbf{r}_{ij}$, and $\mathbf{n}_i$ and $\mathbf{n}_j$ indicating the orientations of particles i and j, respectively. The distance-dependent potentials $U_{\mathrm{R}}(r)$ and $U_{\mathrm{A}}(r)$ are defined as

$$U_{\mathrm{R}}(r)=\varepsilon\left[\left(\frac{r_{\mathrm{min}}}{r}\right)^4-2\left(\frac{r_{\mathrm{min}}}{r}\right)^2\right],\quad r<r_{\mathrm{min}},$$

$$U_{\mathrm{A}}(r) = -\varepsilon \cos^{2\zeta} \frac{\pi(r - r_{\min})}{2(r_{\mathrm{c}} - r_{\min})}, \quad r_{\min} < r < r_{\mathrm{c}},$$

where $r_{\min} = (2)^{1/6}\Sigma$ and $r_{\mathrm{c}} = 2.6\Sigma$. In our MD simulations, ε and Σ are the energy and length units, respectively. The orientation-dependent function is

$$\phi(\hat{\mathbf{r}}_{ij}, \mathbf{n}_i, \mathbf{n}_j) = 1 + \mu[a_\phi(\hat{\mathbf{r}}_{ij}, \mathbf{n}_i, \mathbf{n}_j) - 1],$$

where $a_\phi(\hat{\mathbf{r}}_{ij}, \mathbf{n}_i, \mathbf{n}_j) = (\mathbf{n}_i \times \hat{\mathbf{r}}_{ij}) \cdot (\mathbf{n}_j \times \hat{\mathbf{r}}_{ij}) + (\mathbf{n}_j - \mathbf{n}_i) \cdot \hat{\mathbf{r}}_{ij} \sin\theta_0 - \sin^2\theta_0$.

The function a_ϕ (and consequently ϕ) reaches its maximum value of 1 when the angle between two lipid particles is θ_0, and is less than 1 otherwise. Thus, θ_0 directly correlates with the spontaneous curvature of the membrane.

In summary, the inter-particle pair potentials between the coarse-grained lipid particles in this study are characterized by four parameters: r_{c}, ζ, μ, and θ_0. A typical set of values is $r_{\mathrm{c}} = 2.6$, $\zeta = 4$, $\mu = 3$, and $\theta_0 = 0$ at a temperature $T = 0.23\varepsilon/k_{\mathrm{B}}$, where k_{B} is the Boltzmann constant. The energy ε, length Σ, and mass m for each lipid particle are set to be unity, while the time scale is $\tau = [\varepsilon/(m\Sigma^2)]^{1/2}$. By correlating typical membrane thickness and lateral diffusion observed in experiments, we have the basic length unit $\Sigma \approx 5$ nm and time unit $\tau \approx 0.1$ μs [1, 2].

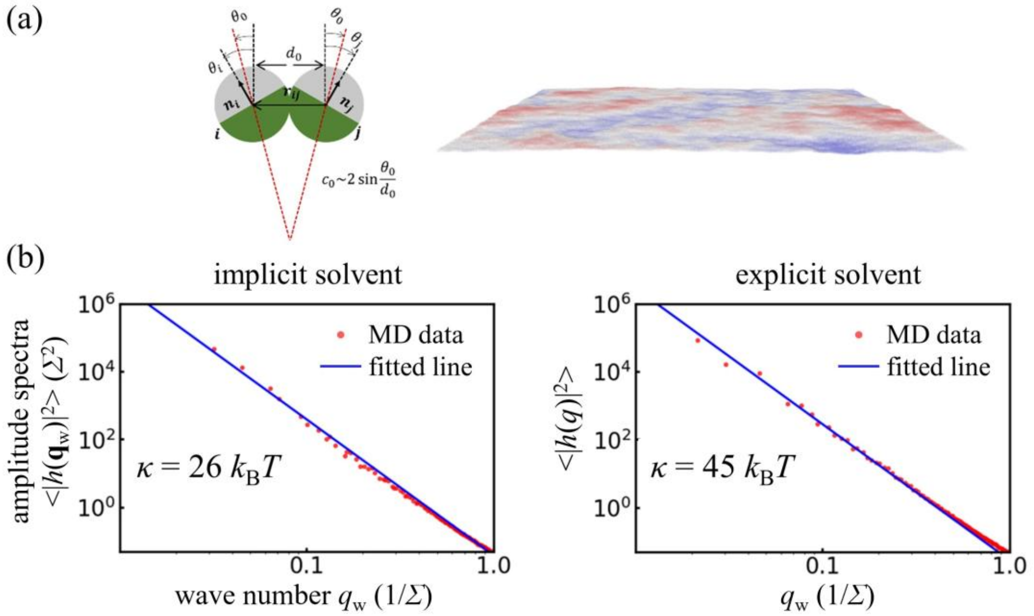

Fig. S1 | Coarse-grained model of lipid membranes. (a) Schematic of the one-particle lipid model alongside a snapshot of a fluctuating lipid membrane. (b) Fitted bending rigidity of the lipid membranes with explicit and implicit solvents.

For vesicles at zero osmotic pressure difference ($\Delta p = 0$), no solvent particles are introduced in the simulations (the implicit solvent model). In contrast, for vesicles maintaining a fixed volume (e.g., reduced volume $v = 0.9$), the explicit solvent model is utilized, which facilitates volume control by adjusting the number of solvent particles within the vesicle.

The interactions among lipid and solvent particles are governed by the 12-6 type Lennard-Jones potential U_{LJ} [2]

$$U_{\mathrm{LJ}}(r) = 4\varepsilon_{\mathrm{p}}\left[\left(\frac{\Sigma_{\mathrm{eq}}}{r}\right)^{12} - \left(\frac{\Sigma_{\mathrm{eq}}}{r}\right)^{6}\right], \quad r < r_{\mathrm{c}}.$$

Here, $\varepsilon_p = 0.2$ is taken for all kinds of particle interactions, with $\Sigma_{eq} = 2.7$ for the solvent-solvent interaction, and $\Sigma_{eq} = 1$ for the solvent-lipid interaction.

Note that the bending rigidity of the lipid membranes varies when solvent particles are introduced, even though the lipid parameters remain consistent. We determine the bending rigidity κ from the membrane fluctuation spectrum, defined as the time-averaged squared modulus of the Fourier-transformed membrane height field $h(\mathbf{q}_w)$ with $\mathbf{q}_w$ as the wavevector and its magnitude $q_w = |\mathbf{q}_w|$ (Fig. S1b). The solvent-free model exhibits a membrane bending rigidity of 26 k_BT, whereas the explicit solvent model results in a bending rigidity of 45 k_BT.

Coarse-grained model of filaments. In the MD simulations, filaments are modeled as chains of coarse-grained particles connected by harmonic bonds and angles of potentials $E_{bond} = k_b(r - r_0)^2$ and $E_{angle} = k_a(\theta - \theta_0)^2$, respectively, where k_b and $r_0 = \Sigma$ denote the bond stiffness and the equilibrium bond distance, respectively; k_a and $\theta_0 = \pi$ are the angle stiffness and the equilibrium angle value (Fig. S2a). The bending stiffness of the filament is primarily governed by the angle stiffness. In this model, the bond stiffness is fixed at a constant value of $1000\varepsilon/\Sigma^2$ for all simulations.

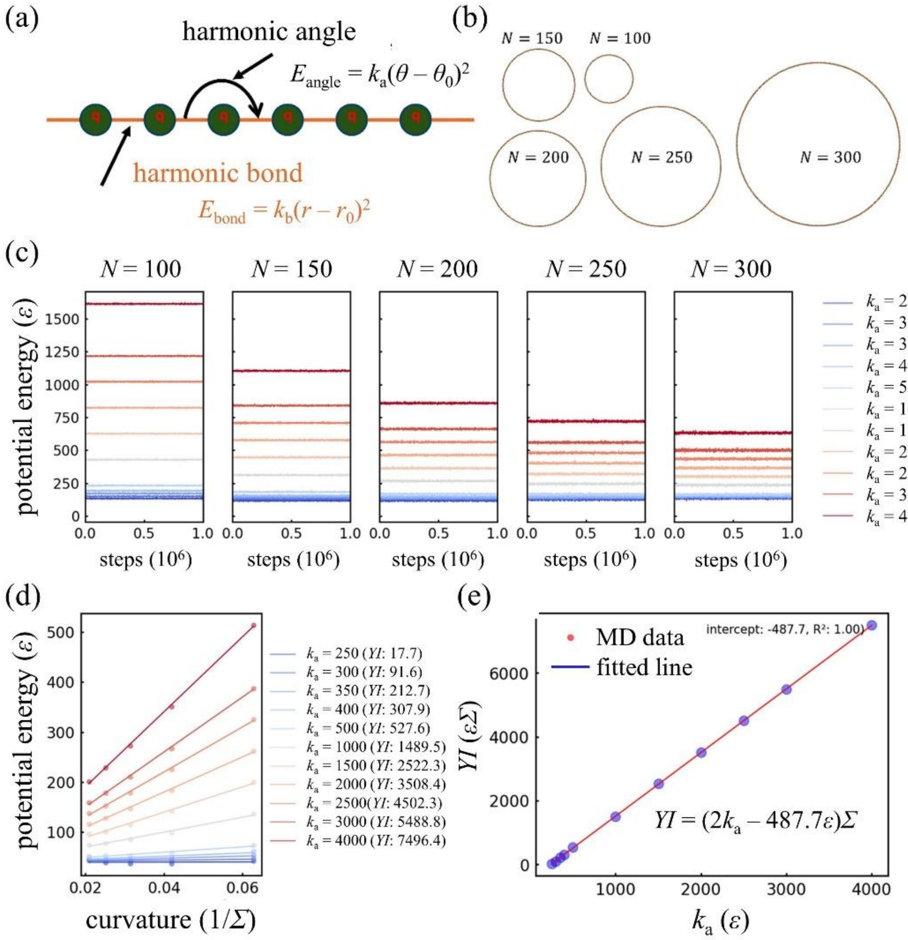

Fig. S2 | Coarse-grained model of filaments. (a) Schematic of the filament model as a chain of particles connected by harmonic bonds and angles. (b) Circular filament rings of varying numbers N of the filament particles. (c) Temporal evolution of the potential energy of filament rings in simulations. (d) Fitted bending stiffness of the filaments, derived from the average potential energy. (e) Fitted linear relationship between the filament bending stiffness and the angle bond stiffness, as determined from the simulations.

To establish the relationship between the bending stiffness of the filament and the angle stiffness, the filaments are bent into circular rings with varying lengths L and angle stiffness values. The system is then relaxed at temperature $T = 0.23\varepsilon/k_B$ for one million steps to achieve equilibrium, as evidenced by the evolution of the potential energy (Fig. S2b,c). The elastic energy of a circular filament ring is given by $E_{\text{filament}} = 2\pi^2 YI/L$, where YI and L represent the bending stiffness and length of the filament, respectively. The slopes in Fig. S2d give the bending stiffness of the filaments, showing that the bending stiffness is linearly dependent on the angle stiffness (Fig. S2e).

To model the electrostatic interaction, each particle of the filament is assigned a unit charge $q = (4\pi\varepsilon_0\varepsilon_r\Sigma)^{1/2}$, resulting in a charge density of $\lambda = qN/(N\Sigma) = (4\pi\varepsilon_0\varepsilon_r/\Sigma)^{1/2}$. The total electrostatic self-interaction energy E_s of a filament ring can be written as

$$E_{\text{s}} = \sum_{i,j=1(i<j)}^{N} \frac{q^2}{4\pi\varepsilon_0\varepsilon_{\text{r}} |\mathbf{r}_{ij}|} = \sum_{i,j=1(i<j)}^{N} \frac{\lambda^2\Sigma^2}{4\pi\varepsilon_0\varepsilon_{\text{r}} |\mathbf{r}_{ij}|},$$

where ε_r is the dielectric constant. The electrostatic interaction is computed using the Particle-Particle Particle-Mesh method [4] with a precision of 10^{-4} in simulations. The electrostatic interaction strength is qualitatively inversely proportional to ε_r for a given system size.

The interactions among lipid, solvent, and filament particles are also governed by the 12-6 type Lennard-Jones potential U_{LJ} described above, where $\varepsilon_p = 0.2$ is applied to all particle interactions, and $\Sigma_{\text{eq}} = 1$ is used for filament-solvent, filament-lipid, filament-filament interactions.

MD simulation protocols–All MD simulations are conducted using the open-sourced software LAMMPS [5] with periodic boundary conditions. The time integration step is set at $\Delta t = 0.005\tau$ for most simulations, and it is reduced to 0.002τ for cases involving large angle stiffness ($k_a > 2000$) to ensure stability in time integration. The vesicle model consists of 33400 lipid particles, corresponding to an approximate radius of 50Σ. To achieve a reduced volume of $v = 0.9$, 10% of the solvent particles within the vesicle are removed using the built-in LAMMPS function ‘fix evaporate’. After equilibrium, the vesicle attains a prolate shape (Fig. S3), consistent with theoretical predictions. In simulations of vesicles at zero osmotic pressure difference, all solvent particles are removed.

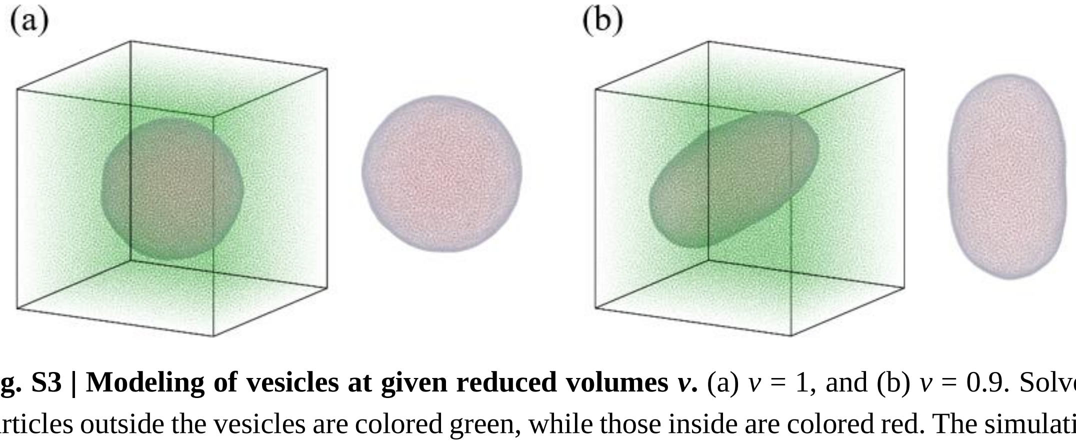

Fig. S3 | Modeling of vesicles at given reduced volumes *v*. (a) $v = 1$, and (b) $v = 0.9$. Solvent particles outside the vesicles are colored green, while those inside are colored red. The simulation box has a size of $b_s = 160\Sigma$.

For the filament–vesicle systems, filaments of varying lengths are positioned inside the vesicle containing solvents, with $k_a = 25$ and $\varepsilon_r = 1$. The system undergoes an initial energy minimization using the conjugate gradient algorithm, with stopping tolerances set at 10^{-4} for energy and 10^{-6}

for force. Following minimization, the solvent is relaxed at a temperature of $T = 0.23\varepsilon/k_B$ using the NPT ensemble (isothermal-isobaric ensemble) for 10^4 steps, after which the temperature of the filament is ramped from $0.02\varepsilon/k_B$ to $0.23\varepsilon/k_B$ in 3×10^4 steps. The entire system is then relaxed for an additional 5×10^5 steps before the production run (Fig. S4a). As detailed in previous sections, the filament stiffness and electrostatic interaction strength are modified based on the angle stiffness k_a and the dielectric constant ε_r. For cases with a reduced volume $v = 0.9$, 10% of the solvent particles inside the vesicle are removed (Fig. S4b). In scenarios involving zero osmotic pressure, all solvent particles are removed. Additionally, for configurations featuring elongated vesicle morphologies, the simulation box size b_s is adjusted to adequately accommodate these morphologies (Fig. S4c). Each system—varying in filament length, stiffness, and electrostatic interaction strength—is simulated for at least 5000τ to ensure equilibrium is achieved. Morphologies of the filament-vesicle system are visualized using OVITO [6]; for clarity, viewing angles are adjusted and solvent particles are not shown in these visualizations in the main text.

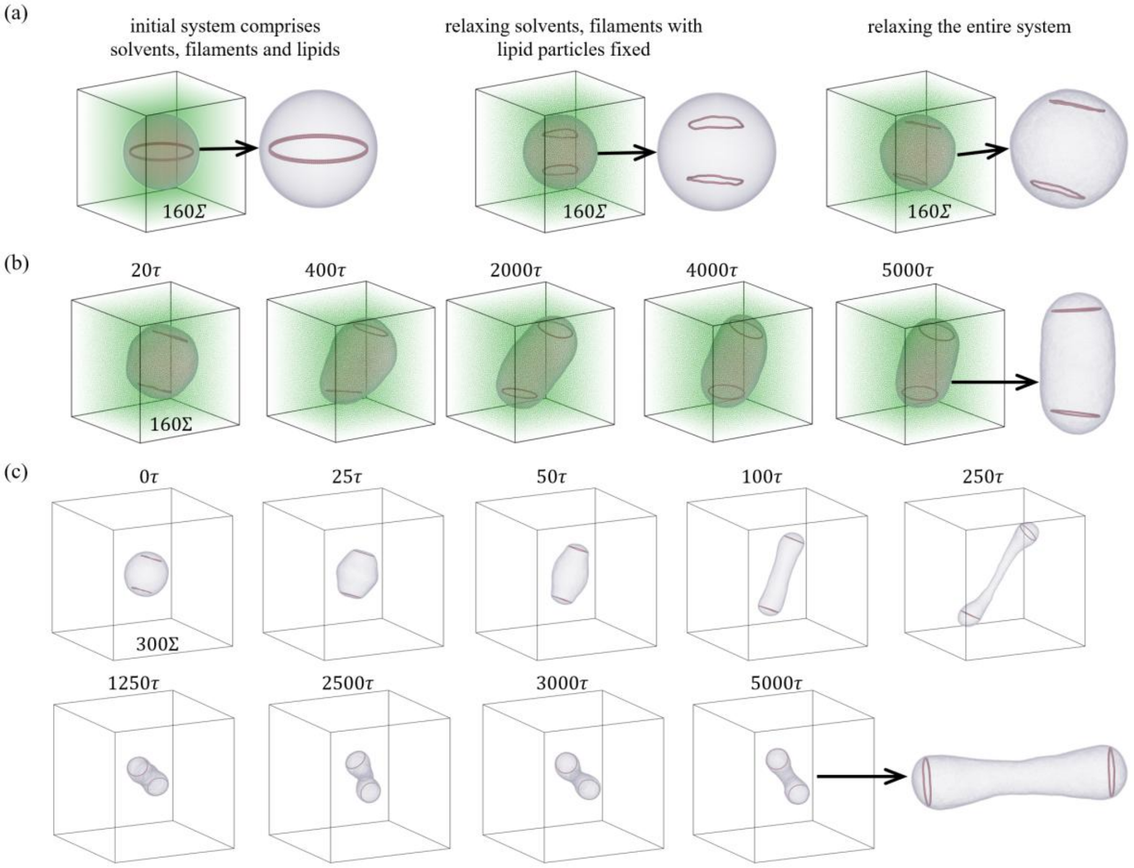

Fig. S4 | Simulation procedures and representative examples. (a) Initial setup of the filaments–vesicle system with normalized filament length 1, angle stiffness $k_a = 25$, and dielectric constant $\varepsilon_r = 1$. The relaxation process includes energy minimization and sequential release of constraints on the solvents, filaments, and lipid membrane within a simulation box of size $b_s = 160\Sigma$. (b) Representative temporal evolution of the filaments–vesicle system at reduced volume $v = 0.9$, with parameters $k_a = 260$ and $\varepsilon_r = 1$. (c) Representative temporal evolution of the filaments–vesicle system under zero osmotic pressure, with an increased box size of $b_s = 300\Sigma$ and parameter values of $k_a = 1700$ and $\varepsilon_r = 0.084$. The final steps highlight the system morphologies with adjusted viewing angles. In panels (a) and (b), solvent particles outside the vesicles are colored green, while those inside are colored red.

Note 3. Numerical and simulation results

At relatively large $L/(\pi R)$ and small χ, the highly flexible filaments slightly deform the confining vesicle at $\Delta p = 0$ (e.g., D_2 morphologies in Fig. 2 in the main text). Using a Cartesian coordinate system centered on the nearly spherical vesicle, the coordinates $\mathbf{r}_i^{\mathrm{f}} = (x_i^{\mathrm{f}},\, y_i^{\mathrm{f}},\, z_i^{\mathrm{f}})$ of filament i can be represented by truncated Fourier series as [7]

$$\begin{aligned}
x_i^{\mathrm{f}} / L &= a\cos\varphi + b\cos[(2k-1)\varphi] + c\cos[(2k+1)\varphi],\\
y_i^{\mathrm{f}} / L &= a\sin\varphi - b\sin[(2k-1)\varphi] + c\sin[(2k+1)\varphi],\\
z_i^{\mathrm{f}} / L &= \delta + \xi\sin(k\varphi).
\end{aligned} \tag{1}$$

Here, a is a reference parameter, b, c, and ξ are the amplitude parameters, k is the integer wave number, φ is the azimuthal angle, and δ is the average z-coordinate of the filaments. When $c = \delta = 0$, $k = 2$, and $\xi = 2(ab)^{1/2}$, Eq. (1) simplifies to a tennis ball seam line curve, which closely approximates the equilibrium configuration of a filament loop constrained to a spherical surface [8]. Performing a perturbation analysis on the filament configuration based on a reference circle, one has two constraint equations

$$|\mathrm{d}\mathbf{r}_i^{\mathrm{f}} / \mathrm{d}\varphi|^2 \approx L^2/(2\pi)^2 \quad \text{and} \quad |\mathbf{r}_i^{\mathrm{f}}|^2 \approx R^2 . \tag{2}$$

Substituting Eq. (1) into Eq. (2) and matching coefficients of constant terms, one obtains

$$\xi^2 = \frac{2}{k^2-1}\left(\frac{1}{4\pi^2} + \delta^2 - \frac{R^2}{L^2}\right), \quad a = \frac{1}{2\pi} - \frac{\pi k^2 \xi^2}{2}, \quad b = \frac{\pi(1+k)^2\xi^2}{8k}, \quad c = -\frac{\pi(1-k)^2\xi^2}{8k}.$$

The saddle-shaped filament configurations suggest that $k = 2$ is the dominant Fourier mode. Once δ is determined, the values of ξ, a, b, and c, as well as the filament configurations, are known. Here, the following power form is adopted for $\delta = \delta(L/(\pi R), \chi)$,

$$\delta = \delta_0 + c_1\left(\frac{L}{\pi R}\right)^{c_2} + c_3\chi^{c_4} + c_5\left(\frac{L}{\pi R}\right)^{c_2}\chi^{c_4}. \tag{3}$$

Eq. (3) well fits the numerical results (Fig. S5). The filament configurations based on Eq. (1) are then obtained and agree well with optimization results (Fig. S6).

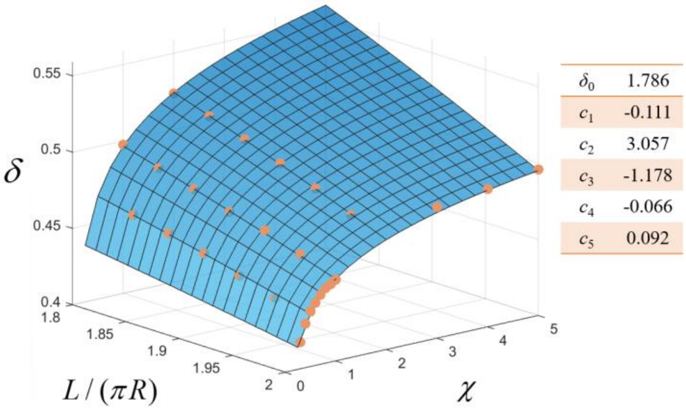

δ_0	1.786
c_1	-0.111
c_2	3.057
c_3	-1.178
c_4	-0.066
c_5	0.092

Fig. S5 | Data points and multivariable regression. The regression of the function δ versus the dimensionless Coulomb interaction strength χ and relative filament length $L/(\pi R)$ for high flexible filaments ($YI/(\kappa R) = 0.1$) in the confining vesicle at $\Delta p = 0$. Values of the fitting parameters are listed in the right table.

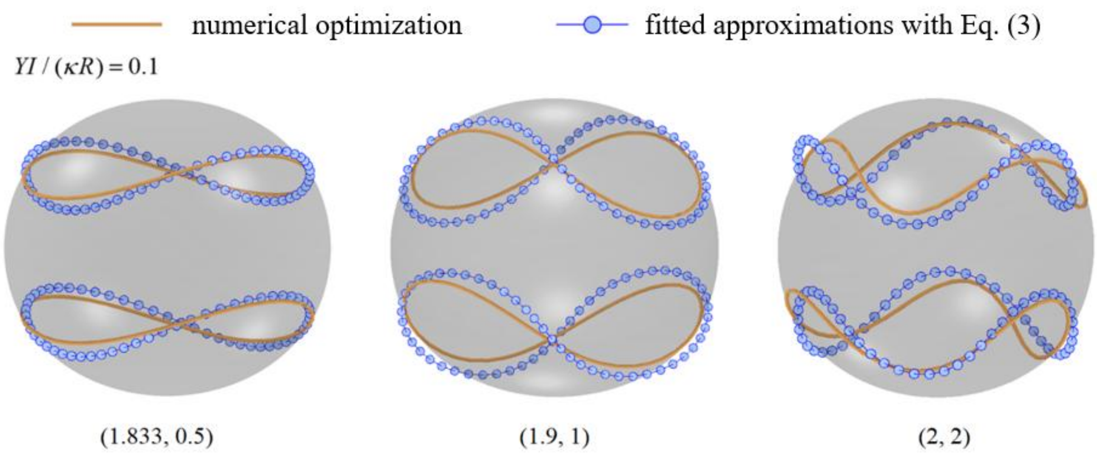

Fig. S6 | System morphology comparison. Morphologies for highly flexible filaments for $YI/(\kappa R) = 0.1$ at $\Delta p = 0$ obtained through numerical optimization and compared with Eq. (3) approximations. The corresponding values of ($L/(\pi R)$, χ) are provided below each morphology. The rightmost morphology with Fourier mode $k = 3$ is energetically metastable.

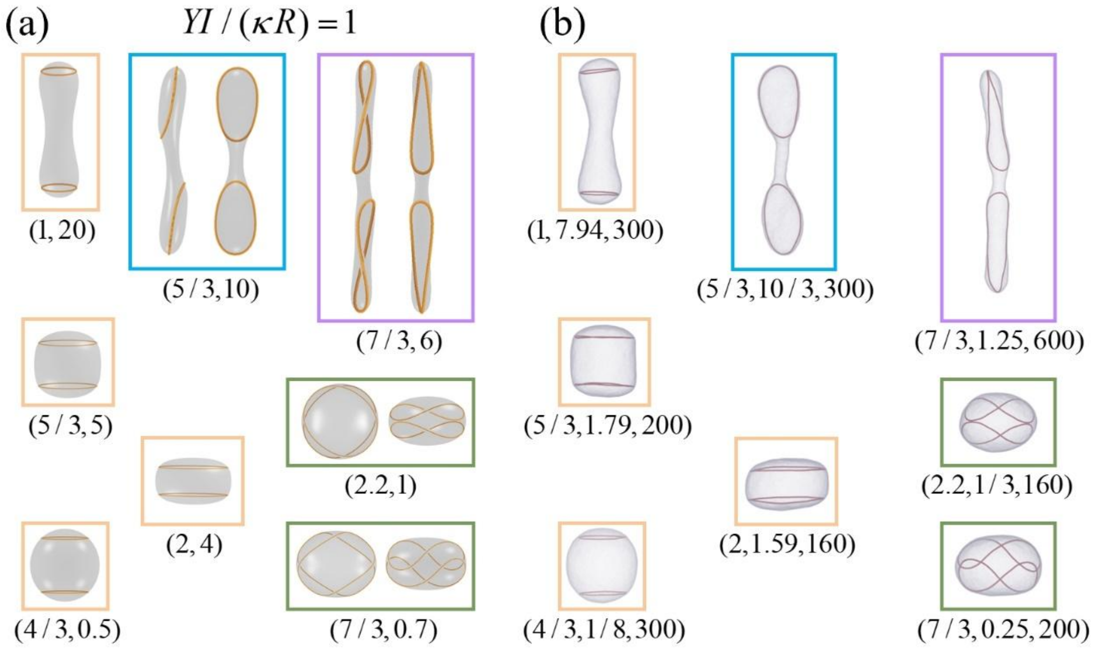

Fig. S7 | Selected equilibrium morphologies of the interacting filaments–vesicle system at $\Delta p = 0$ for $YI/(\kappa R) = 1$ from numerical optimization (a) and MD simulations (b). In panel (a), the respective values of ($L/(\pi R)$, χ) are provided below each morphology. In panel (b), the corresponding values of ($L/(\pi R)$, $1/\varepsilon_r$, b_s/Σ) are displayed, where b_s denotes the simulation box size adjusted to accommodate elongated vesicles. Morphologies within orange frames in (a) are axisymmetric. The length scales in panels (a) and (b) are identical. The morphologies within the orange, green, cyan, and purple frames exhibit $D_{\infty h}$, D_2, C_{2h}, and C_i symmetry, respectively.

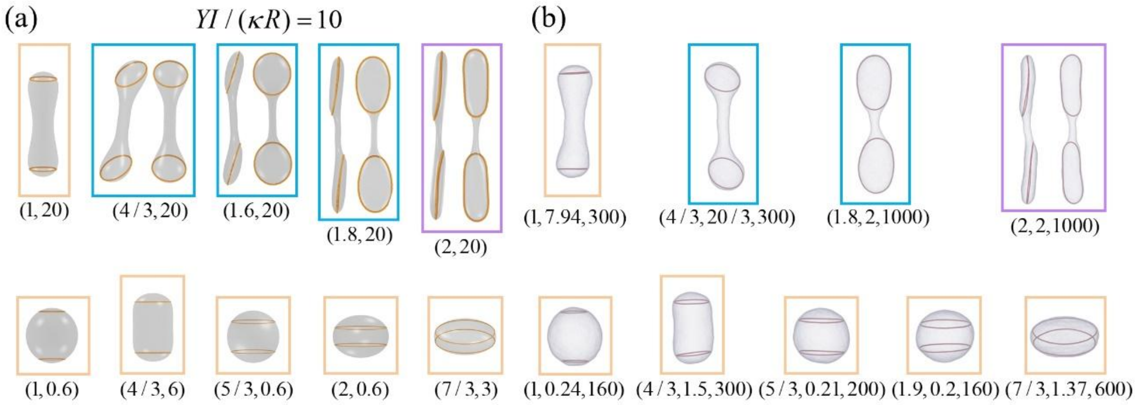

Fig. S8 | Selected equilibrium morphologies of the interacting filaments–vesicle system at Δp = 0 for $YI/(\kappa R)$ = 10 from numerical optimization (a) and MD simulations (b). In panel (a), the respective values of ($L/(\pi R)$, χ) are provided below each morphology. In panel (b), the corresponding values of ($L/(\pi R)$, $1/\varepsilon_r$, b_s/Σ) are displayed, where b_s denotes the simulation box size adjusted to accommodate elongated vesicles. Morphologies within orange frames in (a) are axisymmetric. The length scales in panels (a) and (b) are identical. The morphologies within the orange, green, cyan, and purple frames exhibit $D_{\infty h}$, D_2, C_{2h}, and C_i symmetry, respectively.

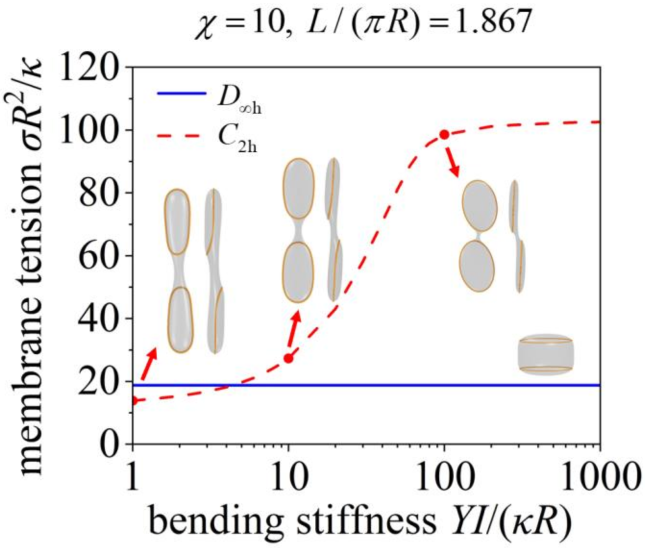

Fig. S9 | Evolution of vesicle membrane tension σ with varying filament bending stiffness, $YI/(\kappa R)$, at $\Delta p = 0$, $\chi = 10$ and $L/(\pi R) = 1.867$. System morphologies at $YI/(\kappa R)$ = 1, 10, and 100 are shown as insets and indicated by arrows.

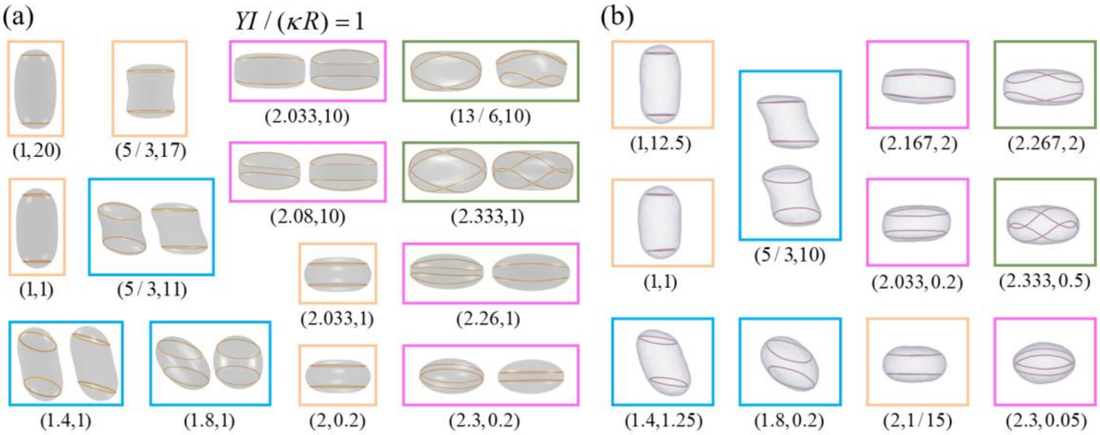

Fig. S10 | Selected equilibrium morphologies of the interacting filaments–vesicle system at v = 0.9 for $YI/(\kappa R)$ = 1 from numerical optimization (a) and MD simulations (b). In (a), the corresponding values of ($L/(\pi R)$, χ) are provided below each morphology, while in (b), the corresponding values of ($L/(\pi R)$, $1/\varepsilon_r$) with the simulation box size b_s = 160Σ are given. Morphologies within orange frames in (a) are axisymmetric. The length scales in panels (a) and (b) are identical.

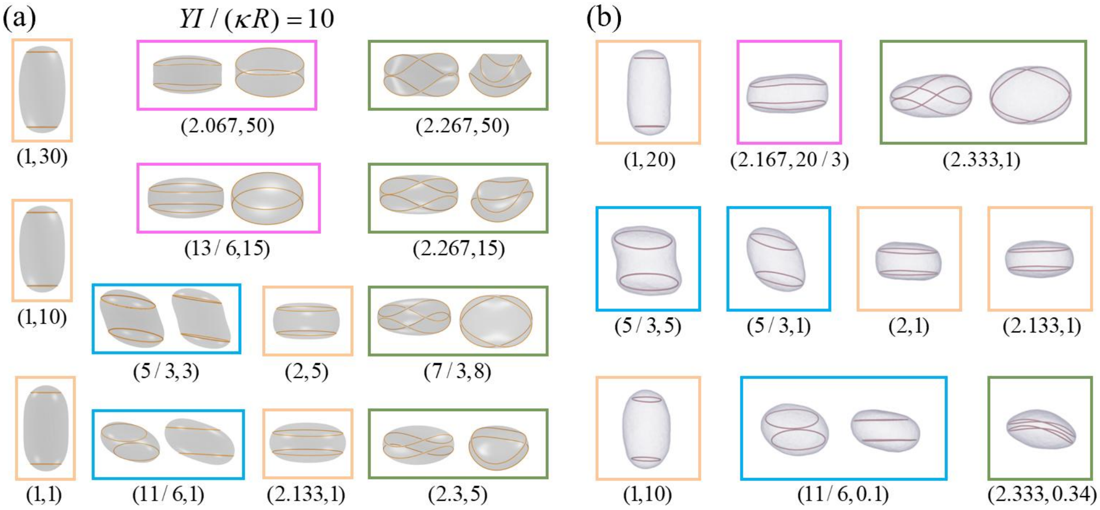

Fig. S11 | Selected equilibrium morphologies of the interacting filaments–vesicle system at v = 0.9 for $YI/(\kappa R)$ = 10 from numerical optimization (a) and MD simulations (b). In (a), the corresponding values of ($L/(\pi R)$, χ) are provided below each morphology, while in (b), the corresponding values of ($L/(\pi R)$, $1/\varepsilon_r$) with the simulation box size b_s = 160Σ are given. Morphologies within orange frames in (a) are axisymmetric. The length scales in panels (a) and (b) are identical.

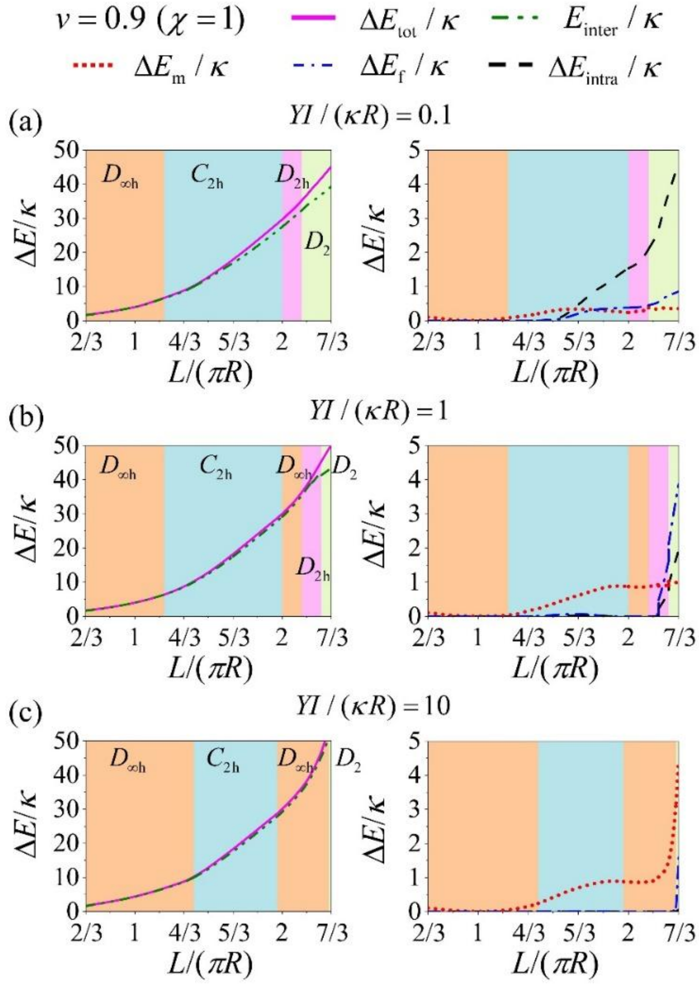

Fig. S12 | Energy component profiles of the charged filaments–vesicle system at v = 0.9 and χ = 1. The relative filament stiffness values are $YI/(\kappa R)$ = 0.1 (a), 1 (b), and 10 (c).

Note 4. Electrostatic interactions with ionic screening effects

This section examines how ionic screening modifies the electrostatic interactions between charged filament segments and affects the resulting morphological behavior of the system. To capture this effect, we extend our model by replacing the bare Coulomb potential with the screened Coulomb potential, which accounts for ionic attenuation in aqueous environments.

By incorporating screened electrostatic interactions, the intrafilament interaction energy E_{intra} and interfilament interaction energy E_{inter} become

$$E_{\text{intra}} = \sum_{i=1,2} \frac{\lambda_i^2}{8\pi\varepsilon_0\varepsilon_{\text{r}}} \int_0^{L_i} \int_0^{L_i} \frac{M(|s_i - \bar{s}_i|) e^{-|\mathbf{r}_i^{\text{f}}(s_i) - \mathbf{r}_i^{\text{f}}(\bar{s}_i)|/\lambda_{\text{D}}}}{|\mathbf{r}_i^{\text{f}}(s_i) - \mathbf{r}_i^{\text{f}}(\bar{s}_i)|} \mathrm{d}s_i \mathrm{d}\bar{s}_i,$$

$$E_{\text{inter}} = \frac{\lambda_1\lambda_2}{4\pi\varepsilon_0\varepsilon_{\text{r}}} \int_0^{L_2} \int_0^{L_1} \frac{e^{-|\mathbf{r}_1^{\text{f}}(s_1) - \mathbf{r}_2^{\text{f}}(\bar{s}_2)|/\lambda_{\text{D}}}}{|\mathbf{r}_1^{\text{f}}(s_1) - \mathbf{r}_2^{\text{f}}(s_2)|} \mathrm{d}s_1 \mathrm{d}s_2.$$

where λ_{D} is the Debye length, quantifying the effective range of electrostatic interactions. It reads $\lambda_{\text{D}} = [4\pi\lambda_{\text{B}}\Sigma(c_{\text{s}}q_{\text{s}}^2)]^{-1/2}$, where λ_{B} is the Bjerrum length, and c_{s} and q_{s} are the concentration and valence of small ions, respectively. At 25 °C and pH 7, pure water's autoionization yields an ionic concentration of approximately 10^{-7} M, giving $\lambda_{\text{D}} \approx 1$ μm and thus minimal electrostatic screening.

Using this screened interaction model with an exponential decay factor, we performed additional numerical simulations to examine how varying screening conditions influence filament conformations and vesicle morphologies. The results, summarized in Fig. S13, reveal the following trends:

(1) Under weak screening (e.g., $\lambda_D/R = 10$), the resulting filament configurations and vesicle shapes are qualitatively similar to those in the unscreened case, demonstrating that the shape transitions remain robust when electrostatic interactions are weakly screened.

(2) Under strong screening ($\lambda_D/R = 0.1$), the effective interfilament repulsion is significantly reduced, which results in a downward shift of the phase boundary and necessitates stronger interaction strength to achieve comparable morphological transitions.

These results provide quantitative insight into how electrostatic screening modulates shape transitions and support the physical intuition that long-range interactions are particularly effective at driving large-scale morphological changes under confinement. While our main model employs unscreened Coulomb interactions to isolate the role of nonlocal repulsion, additional simulations with screened potentials demonstrate that the underlying morphological mechanisms remain robust across a wide range of interaction ranges and decay lengths.

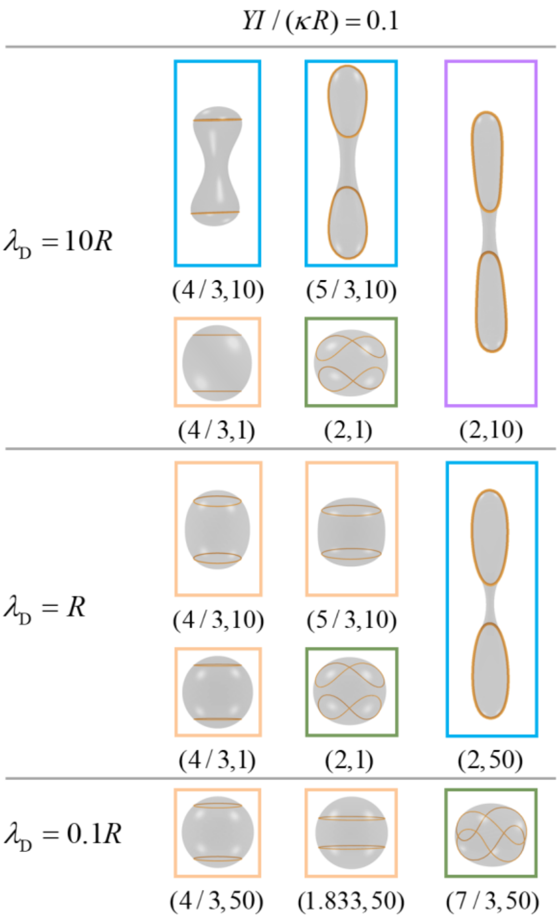

Fig. S13 | Representative equilibrium system morphologies for highly flexible filaments ($YI/(\kappa R) = 0.1$) at different screening lengths $\lambda_D/R = 10$, 1, and 0.1. The corresponding values of $(L/(\pi R), \chi)$ are listed below each morphology.

Note 5. Modeling of magnetically responsive filament systems

Long-range repulsive forces between filaments can also be engineered using magnetically responsive systems. Specifically, we consider a system composed of one paramagnetic filament and one diamagnetic filament. These filaments can be fabricated using established colloidal techniques—for instance, by linking superparamagnetic beads into flexible chains to form the paramagnetic component, and constructing the diamagnetic filament from polymer-coated particles or carbon-based structures.

When placed in an external magnetic field, the paramagnetic filament acquires a magnetic moment aligned with the field, while the diamagnetic filament develops a moment in the opposite direction. This antiparallel dipole alignment along the field axis gives rise to a net repulsive dipole–dipole interaction between the filaments (Fig. S14).

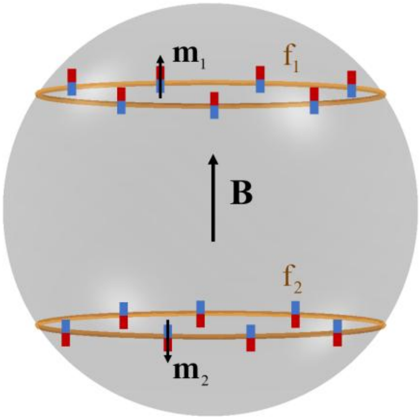

Fig. S14 | Schematic of two magnetically responsive filaments confined within a vesicle. Filament f_1 is paramagnetic, while filament f_2 is diamagnetic. Their oppositely induced magnetic moments lead to a net repulsive dipole–dipole interaction under an external magnetic field of flux density **B**.

Here, we assume that the filament f_1 has a uniform magnetization density $\mathbf{m}_1$ aligned with the magnetic field **B**, while filament f_2 has a uniform magnetization density $\mathbf{m}_2$ anti-aligned with **B**. Both magnetization densities are assumed to have the same constant magnitude $m>0$, such that $\mathbf{m}_1 = m(\mathbf{B}/|\mathbf{B}|)$ and $\mathbf{m}_2 = -m(\mathbf{B}/|\mathbf{B}|)$, where $\mathbf{B}/|\mathbf{B}|$ is the unit vector in the direction of the applied magnetic field.

In general, the magnetic interaction energy between two magnetic dipoles $\mathbf{M}_i$ and $\mathbf{M}_j$ located at positions $\mathbf{r}_i$ and $\mathbf{r}_j$ is given by the dipole–dipole potential [9]

$$E_{\text{dipoles}}^{\text{mag}}(\mathbf{r}_i,\mathbf{r}_j)=\frac{\mu_0}{4\pi|\mathbf{r}_{ji}|^3}\times\left\{\frac{3[(\mathbf{r}_j-\mathbf{r}_i)\cdot\mathbf{M}_i][(\mathbf{r}_j-\mathbf{r}_i)\cdot\mathbf{M}_j]}{|\mathbf{r}_{ji}|^2}-\mathbf{M}_i\cdot\mathbf{M}_j\right\},$$

where μ_0 is the vacuum permeability.

In our case (Fig. S14), both intra- and inter-filament magnetic interactions are computed using this potential as

$$E_{\text{intra}}^{\text{mag}}=\sum_{i=1,2}\frac{\mu_0}{8\pi}\int_0^{L_i}\int_0^{L_i}\frac{M(|s_i-\bar{s}_i|)}{|\mathbf{r}_i^{\text{f}}(s_i)-\mathbf{r}_i^{\text{f}}(\bar{s}_i)|^3}\left[\frac{3\{[\mathbf{r}_i^{\text{f}}(s_i)-\mathbf{r}_i^{\text{f}}(\bar{s}_i)]\cdot\mathbf{m}_i(s_i)\}\{[\mathbf{r}_i^{\text{f}}(s_i)-\mathbf{r}_i^{\text{f}}(\bar{s}_i)]\cdot\mathbf{m}_i(\bar{s}_i)\}}{|\mathbf{r}_i^{\text{f}}(s_i)-\mathbf{r}_i^{\text{f}}(\bar{s}_i)|^2}-\mathbf{m}_i(s_i)\cdot\mathbf{m}_i(\bar{s}_i)\right]\mathrm{d}s_i\mathrm{d}\bar{s}_i,$$

$$E_{\text{inter}}^{\text{mag}}=\frac{\mu_0}{4\pi}\int_0^{L_2}\int_0^{L_1}\frac{1}{|\mathbf{r}_1^{\text{f}}(s_1)-\mathbf{r}_2^{\text{f}}(s_2)|^3}\left[\frac{3\{[\mathbf{r}_1^{\text{f}}(s_1)-\mathbf{r}_2^{\text{f}}(s_2)]\cdot\mathbf{m}_1(s_1)\}\{[\mathbf{r}_1^{\text{f}}(s_1)-\mathbf{r}_2^{\text{f}}(s_2)]\cdot\mathbf{m}_2(s_2)\}}{|\mathbf{r}_1^{\text{f}}(s_1)-\mathbf{r}_2^{\text{f}}(s_2)|^2}-\mathbf{m}_1(s_1)\cdot\mathbf{m}_2(s_2)\right]\mathrm{d}s_1\mathrm{d}s_2.$$

In Fig. S15, we systematically explore the equilibrium configurations of vesicles containing magnetic filaments of bending stiffness $YI/(\kappa R) = 10$. Our results demonstrate that magnetic interactions between filaments can qualitatively reproduce the same spectrum of vesicle deformation—such as elongation, flattening, and neck formation—that closely resemble those induced by long-range electrostatic repulsion discussed in the main text. These findings suggest that directional repulsion arising from magnetic contrast (e.g., between paramagnetic and diamagnetic components) can serve as an effective surrogate for nonlocal filament–filament repulsion, offering a viable route for experimental realization through magnetic design.

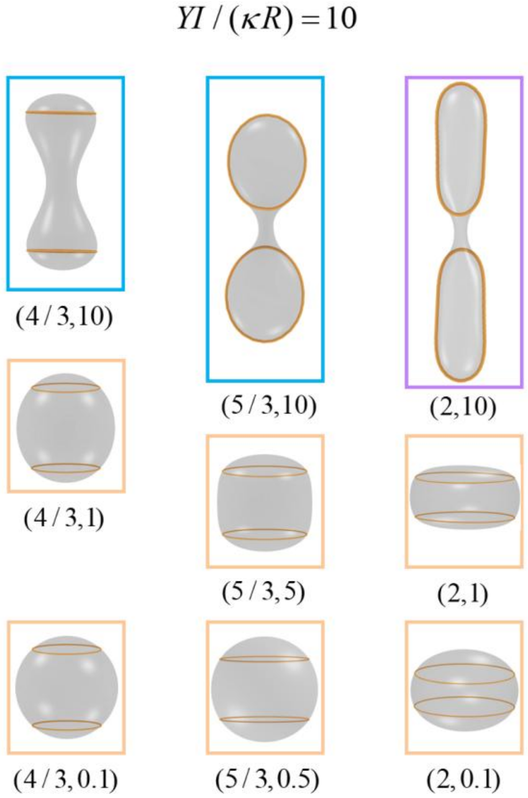

Fig. S15 | Magnetically responsive filaments–vesicle system for filaments of $YI/(\kappa R) = 10$ at $\Delta p = 0$. Representative system morphologies in equilibrium obtained from numerical optimization, with the corresponding values of $(L/(\pi R), \eta)$ provided below each image. Here, $\eta = \mu_0 m^2/(4\pi R\kappa)$ denotes the dimensionless magnetic interaction strength.

References

1. Yuan, H., Huang, C., Li, J., Lykotrafitis, G. & Zhang, S. One-particle-thick, solvent-free, coarse-grained model for biological and biomimetic fluid membranes. *Phys. Rev. E* **82**, 011905 (2010).
2. Fu, S.-P., Peng, Z., Yuan, H., Kfoury, R. & Young, Y.-N. Lennard-Jones type pair-potential method for coarse-grained lipid bilayer membrane simulations in LAMMPS. *Comput. Phys. Commun*. **210**, 193–203 (2017).
3. Liu, Y., Zou, G. & Gao, H. Domain aggregation and associated pore growth in lipid membranes. *ACS Nano* **15**, 604–613 (2021).

4. Eastwood, J. W., Hockney, R. W. & Lawrence, D. N. P3M3DP—the three-dimensional periodic particle-particle/particle-mesh program. *Comput. Phys. Commun*. **19**, 215–261 (1980).
5. Plimpton, S. Fast parallel algorithms for short-range molecular dynamics. *J. Comput. Phys.* **117**, 1–19 (1995).
6. Stukowski, A. Visualization and analysis of atomistic simulation data with OVITO—the Open Visualization Tool. *Modell. Simul. Mater. Sci. Eng*. **18**, 015012 (2009).
7. Alben, S. Packings of a charged line on a sphere. *Phys. Rev. E* **78**, 066603 (2008).
8. Wang, M., Li, X. & Yi, X. Deformation, shape transformations, and stability of elastic rod loops within spherical confinement. *J. Mech. Phys. Solids* **191**, 105771 (2024).
9. Sano, T. G. Reduced theory for hard magnetic rods with dipole–dipole interactions. *J. Phys. A: Math. Theor*. **55**, 104002 (2022).